Available online at www.sciencedirect.com

ScienceDirect

Underground Space 21 (2025) 331–351

www.keaipublishing.com/undsp

Research Paper

Analysis of the dynamic response and damage characteristic for the tunnel under near-field blasts and far-field earthquakes

Hao Luo [a], Ming Tao [a,*], Zhixian Hong [a], Gongliang Xiang [a], Chengqing Wu [b]

[a] School of Resources and Safety Engineering, Central South University, Changsha 410083, China
[b] School of Civil and Environmental Engineering, University of Technology Sydney, Ultimo 2007, Australia

Received 23 July 2024; received in revised form 9 September 2024; accepted 16 September 2024
Available online 30 November 2024

Abstract

The dynamic response and failure characteristics of tunnels vary significantly under various dynamic disturbances. These characteristics are crucial for assessing structural stability and designing effective support for surrounding rock. In this study, the theoretical solution for the dynamic stress concentration factor (DSCF) of a circular tunnel subjected to cylindrical and plane P-waves was derived using the wave function expansion method. The existing equivalent blast stress wave was optimized and the Ricker wavelet was introduced to represent the seismic stress waves. By combining Fourier transform and Duhamel's integral, the transient response of the underground tunnel under near-field blasts and far-field earthquakes was determined in both the frequency and time domains. The theoretical results were validated by comparing them with those obtained from numerical simulations using ANSYS LS-DYNA software. Numerical simulations were conducted to further investigate the damage characteristics of the underground tunnel and evaluate the effect of initial stress on structural failure under both types of disturbances. The theoretical and numerical simulation results indicated that the differences in the dynamic response and damage characteristics of the underground tunnel were primarily due to the curvature of the stress waves and transient load waveform. The locations of the maximum DSCF values differed between near-field blasts and far-field earthquakes, whereas the minimum DSCF values occurred at the same positions. Without initial stress, the blast stress waves caused spalling damage to the rock mass on the wave-facing side. Shear failure occurred near the areas with maximum DSCF values, and tensile failure occurred near the areas with minimum DSCF values. In contrast, damage occurred only near the areas with maximum DSCF values under seismic stress waves. Furthermore, the initial stress exacerbated spalling and shear damage while suppressing tensile failure. Hence, the blast stress waves no longer induced tensile failure on the tunnel sidewalls under initial stress.

Keywords: Dynamic response; Damage characteristics; Underground tunnel; Near-field blasts; Far-field earthquakes; Initial stress

1 Introduction

As underground construction and resource extraction progressively reach deeper into the earth, the demand for constructing underground tunnels and mining roadways significantly increases over the years. Deep tunnels are situated in complex stress environments under the influence of geological structures, high in-situ stresses, and dynamic disturbances such as blasting, earthquakes, and unloading, where structural damage and failure of tunnels occur frequently (Gu et al., 2023; Jeon et al., 2004; Luo et al., 2023). For instance, intensive rockbursts occurred during tunnel blasting excavation at the Jinping II hydropower station, China (Su et al., 2017), and excavation disturbances induced spalling damage at the Baihetan hydropower station, China (Jiang et al., 2013). In addition, the earthquakes in Wenchuan, Norcia, and Kumamoto caused significant damage to both underground and mountain tunnels (Callisto & Ricci, 2019). All of these phenomena can be categorized as dynamic disasters in deep

* Corresponding author.
E-mail address: mingtao@csu.edu.cn (M. Tao).
Peer review under the responsibility of Tongji University.

https://doi.org/10.1016/j.undsp.2024.09.003

underground engineering caused by transient disturbances, which involve stress wave scattering, dynamic stress concentrations, and structural failure mechanisms. Therefore, investigating the dynamic response and failure characteristics of underground structures under transient disturbances is fundamental to ensure the safe extraction of deep resources and development of underground spaces.

After decades of research, theoretical calculation methods, experimental techniques, and numerical simulation methods for stress wave scattering and dynamic stress concentrations have advanced significantly, and they have been widely applied in deep resource extraction and underground space engineering. Pao and Mow (1973) systematically summarized the derivation process for the steady-state response of circular and elliptical cavities under P-wave and S-wave incidence using the wave function expansion method. They provided the theoretical expression for the dynamic stress concentration factor (DSCF). Subsequently, Liu et al. (1980) were the first to introduce the complex variable function theory and conformal transformation into the process of solving stress wave scattering in discontinuous structures and derived the numerical solution expressions for the DSCF around cavities with arbitrary cross sections. Lee and Karl (1992) applied large circular arc approximation to the problem of scattering around shallow-buried cavities under SV-wave action, providing new insights and methods for analyzing semi-infinite space theoretical models. Furthermore, the effects of different burial depths on the stress and deformation around shallow-buried cavities were discussed. Liu et al. (2017) employed the indirect boundary integration equation method to investigate the DSCF distribution around a lined tunnel subjected to P-wave incidence in a fluid-saturated poroelastic half-space. Significant progress has been achieved in studying the transient response of underground structures. Tao et al. (2019) combined the complex variable function method with Fourier transform to determine the spatial distribution characteristics of the transient DSCF for shallow-buried and deep-buried tunnels under P-wave incidence. Xia et al. (2017) obtained the stress variation characteristics of a cylindrical casing-cement structure in a poroelastic stratum under transient loading based on Biot's theory and inverse Laplace transforms.

Dynamic failure of underground structures has also garnered the interest of many researchers. Li and Li (2018) employed the discrete element method (DEM) software PFC to investigate the damage characteristics of underground tunnels under the combined effects of in-situ stress and dynamic blasting loads. The influence of the failure mode of underground tunnels on the wavelength-to-tunnel-diameter ratio and in-situ stress was evaluated. Wang et al. (2020) used the 3DEC DEM software to analyze the stability of large underground powerhouse caverns, and they studied the random block stability, seismic dynamic response, and rock support system through the calculation of three typical engineering scenarios. Elgamal and Elfaris (2022) used the MIDAS GTS NX finite element method (FEM) software to conduct a detailed analysis of tunnel behavior under seismic shaking and the response with seismic isolation measures. Li and Chen (2020) used ABAQUS FEM software to perform three-dimensional nonlinear simulations of the seismic behavior of a subway station, considering the effects of vertical ground motion and structural overburden depth. Mitelman and Elmo (2014) proposed a hybrid finite-discrete element method to investigate tunnel damage induced by blasting, and this method was used to study the influence of rock strength properties on the durability of tunnels subjected to blast loads.

The transient disturbances that pose the greatest risk to underground structures are primarily excavation blasting and natural earthquakes. Blast stress waves have limited duration, high vibration frequencies, and short wavelengths, which affect tunnels in the form of cylindrical waves. In contrast, seismic stress waves have low vibration frequencies, high energies, and long propagation paths and durations. When seismic stress waves propagate near tunnels, they can be considered as plane waves. Investigating the stress distribution characteristics and assessing the stability of tunnels under blast and seismic loadings has considerable engineering significance and practical value. Therefore, this study is primarily focused on differential analysis of the dynamic response and damage characteristics of underground tunnel subjected to near-field blast and far-field earthquake waves. The equivalent blast waveform was improved to reflect the actual blast stress waves more accurately, and the Ricker wavelet was introduced to represent the seismic loads. Subsequently, based on the wave function expansion method, Duhamel's integral and Fourier transform were employed to determine the transient DSCF distribution of the tunnel in the time and frequency domains, respectively. The effects of tunnel radius, blast source distance, disturbance wavelength, and Poisson's ratio were evaluated. The reliability of the theoretical results was validated using FEM simulations. Finally, a deep-buried tunnel numerical model with initial stress was established using ANSYS LS-DYNA software to further investigate the dynamic damage characteristics of the structure. The aim of this study is to provide theoretical guidance for seismic and blast-resistant design of underground tunnels.

2 Theoretical model and parameterization

The main blast disturbances in underground tunnels originate from the blasting construction in adjacent tunnels, resource drilling, and blasting extraction. The blast stress waves propagate to the tunnel in the form of cylindrical waves. Earthquake sources typically exist at depths ranging from ten kilometers to several tens of kilometers underground. When the seismic stress waves reach the tunnel, their curvatures approach zero, allowing them to be treated as plane waves. A theoretical model of an underground tunnel subjected to disturbances from near-field

blasts and far-field seismic waves is shown in Fig. 1. It was assumed that the tunnel was located in an elastic rock mass in infinite space, with the elastic properties of the rock mass determined by the elastic modulus E, Poisson's ratio ν, and density ρ. The distance between the existing tunnel and blast source is denoted as r_0, while the radii of the existing and adjacent tunnels are represented by a and $\bar{a}$, respectively. In addition, the angular coordinates in the two cylindrical coordinate systems are designated as θ and $\bar{\theta}$.

According to the tunnel cross-sectional area classification standards defined by the International Tunnelling and Underground Space Association (ITA), tunnels can be categorized into small-section (3–10 m^2), medium-section (10–50 m^2), and large-section (50–100 m^2) tunnels. To make the theoretical model more representative of an actual tunnel, the existing tunnel radius a was set at 1, 3 and 5 m, corresponding to three types of tunnel. In traffic engineering, the distance between two tunnels typically ranges from 5 to 10 m. To investigate the effect of the blast source distance r_0 on the blast response of the tunnel, r_0 was set at $3a$, $5a$, and $10a$, corresponding to close, medium, and long blast source distances, respectively. There is a marked difference between the wavelengths of the blast and seismic waves. The blast wave wavelengths vary from several meters to tens of meters, whereas the seismic wave wavelengths range from tens of meters to several kilometers. To better study the effects of the transient disturbance wavelengths on the dynamic response, the passage time of the stress waves through the tunnel was normalized. The dimensionless time t_D is defined as the ratio of the wavelength of the stress wave to the radius of the existing tunnel during duration t, and can be expressed as

$$t_D = \frac{c_p t}{a}, \tag{1}$$

where c_p is the P-wave velocity and $c_p = \sqrt{E/\rho}$.

Considering the differences in the wavelength ranges between the seismic and blast waves, the wavelengths of seismic waves were significantly larger than those of blast waves. Based on the definition of dimensionless time, the t_D for blast waves were set at 5, 10, and 15, whereas the t_D for seismic waves were set at 25, 50, and 100.

3 Near-field blast model

3.1 Governing equations of the wave field

To analyze the blast response of tunnels, it is essential to obtain the steady-state response of the cylindrical waves. The primary distinction between cylindrical and plane waves lies in the curvature of the cylindrical waves, which is directly governed by the blast source distance. In cylindrical coordinates (r, θ) and $(\bar{r}, \bar{\theta})$, the incident blast wave can be expressed as an infinite series sum using the wave function expansion method (Pao & Mow, 1973):

$$\begin{aligned}\varphi_B^{(i)} &= \varphi_0 H_0^{(1)}(\alpha\bar{r})e^{i(\alpha x-\omega t)} \\ &= \varphi_0 \sum_{n=0}^{\infty}(-1)^n \varepsilon_n J_n(\alpha r) H_n^{(1)}(\alpha r_0)\cos(n\theta)e^{-i\omega t},\end{aligned} \tag{2}$$

where $\varphi_B^{(i)}$ is the potential function of the blast incident wave, $\bar{r} = \sqrt{a^2 + r_0^2 + 2ar_0\cos\theta}$, $\varepsilon_n = \begin{cases} 1, & n = 0 \\ 2, & n \geq 1 \end{cases}$, and φ_0 and α represent the amplitude of displacement potential function and wave number of incident wave, respectively. The wave number α is defined as the ratio of circular frequency ω to the P-wave velocity c_p. $J_n(\alpha r)$ and $H_n^{(1)}(\alpha r)$ denote the first Bessel function and Hankel function, respectively.

Owing to the presence of the tunnel, the propagation of stress waves exhibits scattering as the waves pass through the tunnel, resulting in scattered P-waves and SV-waves. These can be represented as follows (Pao & Mow, 1973):

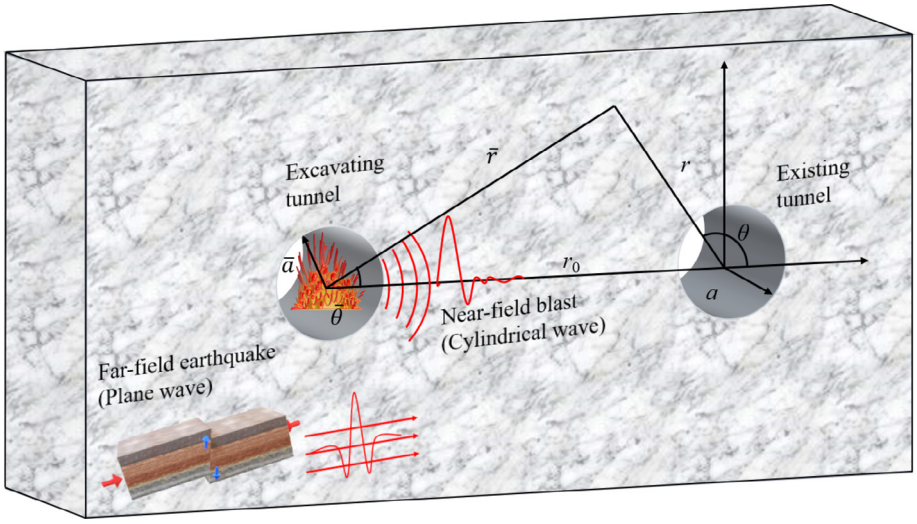

Fig. 1. Schematic of the underground tunnel subjected to near-field blasts and far-field earthquakes.

$$\varphi_{\mathrm{B}}^{(\mathrm{s})}=\sum_{n=0}^{\infty}A_n^{\mathrm{B}}H_n^{(1)}(\alpha r)\cos(n\theta)\mathrm{e}^{-\mathrm{i}\omega t}, \tag{3}$$

$$\psi_{\mathrm{B}}^{(\mathrm{s})}=\sum_{n=0}^{\infty}B_n^{\mathrm{B}}H_n^{(1)}(\beta r)\sin(n\theta)\mathrm{e}^{-\mathrm{i}\omega t}, \tag{4}$$

where $\varphi_{\mathrm{B}}^{(\mathrm{s})}$ is the potential function of the scattered P-waves, $\psi_{\mathrm{B}}^{(\mathrm{s})}$ is the potential function of the scattered SV-waves, A_n^{B} and B_n^{B} are the undetermined expansion coefficients, β is the wavenumber of the scattered SV-wave and $\beta=\omega/c_{\mathrm{s}}$, and c_{s} is the S-wave velocity.

According to the superposition principle of stress waves, the full wave in the rock mass can be written as

$$\varphi_{\mathrm{B}}^{(\mathrm{f})}=\sum_{n=0}^{\infty}\left[\varphi_0(-1)^n\varepsilon_nJ_n(\alpha r)H_n^{(1)}(\alpha r_0)+A_n^{\mathrm{B}}H_n^{(1)}(\alpha r)\right]\cos(n\theta)\mathrm{e}^{-\mathrm{i}\omega t}, \tag{5}$$

$$\psi_{\mathrm{B}}^{(\mathrm{f})}=\sum_{n=0}^{\infty}B_n^{\mathrm{B}}H_n^{(1)}(\beta r)\sin(n\theta)\mathrm{e}^{-\mathrm{i}\omega t}, \tag{6}$$

where $\varphi_{\mathrm{B}}^{(\mathrm{f})}$ is the potential function of the full P-waves, and $\psi_{\mathrm{B}}^{(\mathrm{f})}$ is the potential function of the full S-waves.

After deriving the expression for the full wave field function in the rock mass, the stress distribution around the tunnel can be determined using the relationship between the displacement potential and stress. The expressions for the three types of surrounding rock stresses are presented as follows (Li et al., 2016):

$$\sigma_{rr}^{\mathrm{B}}=\frac{2\mu}{R^2}\times\sum_{n=0}^{\infty}\left[(-1)^n\varepsilon_n\varphi_0H_n^{(1)}(\alpha r_0)\varepsilon_{11}^{(1)}+A_n^{\mathrm{B}}\varepsilon_{11}^{(3)}+B_n^{\mathrm{B}}\varepsilon_{12}^{(3)}\right]\cos(n\theta)\mathrm{e}^{-\mathrm{i}\omega t}, \tag{7}$$

$$\sigma_{r\theta}^{\mathrm{B}}=\frac{2\mu}{R^2}\times\sum_{n=0}^{\infty}\left[(-1)^n\varepsilon_n\varphi_0H_n^{(1)}(\alpha r_0)\varepsilon_{41}^{(1)}+A_n^{\mathrm{B}}\varepsilon_{41}^{(3)}+B_n^{\mathrm{B}}\varepsilon_{42}^{(3)}\right]\sin(n\theta)\mathrm{e}^{-\mathrm{i}\omega t}, \tag{8}$$

$$\sigma_{\theta\theta}^{\mathrm{B}}=\frac{2\mu}{R^2}\times\sum_{n=0}^{\infty}\left[(-1)^n\varepsilon_n\varphi_0H_n^{(1)}(\alpha r_0)\varepsilon_{21}^{(1)}+A_n^{\mathrm{B}}\varepsilon_{21}^{(3)}+B_n^{\mathrm{B}}\varepsilon_{22}^{(3)}\right]\cos(n\theta)\mathrm{e}^{-\mathrm{i}\omega t}, \tag{9}$$

where $\varepsilon_{11}^{(1)}$, $\varepsilon_{11}^{(3)}$, and $\varepsilon_{12}^{(3)}$, etc. denote the contribution factors of various stress wave types to the stress surrounding the tunnel, all of which are presented in the Appendix. In addition, R and μ represent the distance to the center of the existing tunnel and the shear modulus of the rock mass, respectively.

The tunnel boundary is a traction-free boundary condition, which can be expressed as follows:

$$\begin{cases}\sigma_{rr}^{\mathrm{B}}\big|_{r=a}=0\\ \sigma_{r\theta}^{\mathrm{B}}\big|_{r=a}=0\end{cases}. \tag{10}$$

Hence, the undetermined expansion coefficients can be obtained by substituting Eqs. (7) and (8) into Eq. (10), which can be represented as

$$A_n^{\mathrm{B}}=(-1)^{n+1}\varphi_0\varepsilon_nH_n^{(1)}(\alpha r_0)\frac{\begin{vmatrix}E_{11}^{(1)}&E_{12}^{(3)}\\E_{41}^{(1)}&E_{42}^{(3)}\end{vmatrix}}{\begin{vmatrix}E_{11}^{(3)}&E_{12}^{(3)}\\E_{41}^{(3)}&E_{42}^{(3)}\end{vmatrix}}, \tag{11}$$

$$B_n^{\mathrm{B}}=(-1)^{n+1}\varphi_0\varepsilon_nH_n^{(1)}(\alpha r_0)\frac{\begin{vmatrix}E_{11}^{(3)}&E_{11}^{(1)}\\E_{41}^{(3)}&E_{41}^{(1)}\end{vmatrix}}{\begin{vmatrix}E_{11}^{(3)}&E_{12}^{(3)}\\E_{41}^{(3)}&E_{42}^{(3)}\end{vmatrix}}, \tag{12}$$

where $E_{11}^{(1)}$, $E_{11}^{(3)}$, $E_{12}^{(3)}$, etc. are the values of $\varepsilon_{11}^{(1)}$, $\varepsilon_{11}^{(3)}$, $\varepsilon_{12}^{(3)}$, etc., at $r=a$.

Subsequently, the values of the undetermined expansion coefficients were substituted into Eq. (9) to obtain the stress distribution around the tunnel. To quantitatively describe the surge in stress in the tunnel surrounding rock, the DSCF was employed to examine the characteristics of the stress variation around the tunnel. The maximum radial stress σ_0^{B} and $\mathrm{DSCF_B}$ resulting from the cylindrical P-waves can be expressed as follows:

$$\begin{cases}\sigma_0^{\mathrm{B}}=\alpha^2\mu\varphi_0\left[H_2^{(1)}(\alpha\bar{r})+(1-\kappa^2)H_0^{(1)}(\alpha\bar{r})\right]\\ \mathrm{DSCF_B}=\frac{\sigma_{\theta\theta}^{\mathrm{B}}}{\sigma_0^{\mathrm{B}}}=\frac{2}{\alpha^2\bar{r}^2}\frac{\sum_{n=0}^{\infty}(-1)^n\varepsilon_nH_n^{(1)}(\alpha r_0)\left[\varepsilon_{21}^{(1)}-A_n^{\mathrm{B}}\varepsilon_{21}^{(3)}-B_n^{\mathrm{B}}\varepsilon_{22}^{(3)}\right]\mathrm{e}^{-\mathrm{i}\omega t}\cos(n\theta)}{H_2^{(1)}(\alpha\bar{r})+(1-\kappa^2)H_0^{(1)}(\alpha\bar{r})}\end{cases}, \tag{13}$$

where κ is the ratio of the wavenumber of S-waves to that of P-waves and $\kappa=\frac{\beta}{\alpha}$.

3.2 Blast loading and Duhamel's integral

Previous studies have often employed a half-sine wave to approximate the blast stress waves. In practical engineering applications, the ascending duration of the blast stress wave is significantly shorter than its subsequent descent, whereas a half-sine wave features identical durations for both the ascending and descending phases. Hence, Tao et al. (2020) proposed an equivalent blast wave, where the ascending and descending duration of the stress waves can be adjusted by controlling the ascent ratio (AR). The measured blast stress waves typically exhibit a rapid ascent to a maximum, followed by a gradual descent to a minimum value below zero, and finally a gradual ascent back to zero. Neither of the two aforementioned stress wave types considers the reverse tensile part of the actual blast stress wave. Therefore, an optimized equivalent blast wave was proposed in this study that supplemented a reverse

tensile load into the base model and adjusted the AR to ensure that the waveform of the optimized model closely mirrored that of the actual blast wave. The three types of blast waveform are shown in Fig. 2.

Lu et al. (2012) discovered that the ascending duration of the blast stress wave was primarily determined by the detonation wave velocity, whereas the descending duration was primarily dependent on the elastic wave velocity of the rock mass. The velocity of the detonation wave is typically approximately twice that of the elastic wave. Consequently, the AR for the optimized equivalent blast wave was set at 1/3. The optimized equivalent blast wave is given by

$$f(t)=\begin{cases} \mathrm{e}^{\frac{C}{D}\arctan\left(\frac{D}{C}\right)}\sqrt{1+\left(\frac{C}{D}\right)^2}\cdot \mathrm{e}^{-Ct}\cdot \sin\left(Dt\right),\ 0\le t<t_0 \\ 0\ ,\ t\ge t_0 \end{cases}, \tag{14}$$

where t_0 denotes the period of the equivalent blast wave, t_1 denotes the peak time, and $D=2\pi/t_0$, $C=D\cot(Bt_1)$, and AR = $2t_1/\ t_0$ denote the control parameters.

To obtain the transient response of the tunnel subjected to near-field blasts, it is necessary to employ Duhamel's integral to establish a connection between the steady-state and transient responses. By introducing the Dirac delta function and Heaviside step function, Duhamel's integral correlates the blast load at each moment with the steady-state response in the time domain. This method superimposes dynamic responses in the time domain, thereby yielding the transient DSCF of the tunnel. The transient response can be written as (Xiang et al., 2024)

$$g(\chi,t)=\begin{cases} \frac{2}{\pi}\int_0^{\infty}\frac{\chi(x,\omega)}{\omega}\cdot[G(t)]\mathrm{d}\omega,\ 0\le t<t_0 \\ \frac{2}{\pi}\int_0^{\infty}\frac{\chi(x,\omega)}{\omega}\cdot[G(t_0)]\mathrm{d}\omega,\ t\ge t_0 \end{cases}, \tag{15}$$

where $\chi(\omega)$ is the steady-state response of the tunnel subjected to simple harmonic waves and $G(t)$ is the integral expression of the input excitation function. The integral of the equivalent blast wave is expressed as follows:

$$\begin{cases} G(t)=\int_0^t f'(\tau)\cdot\sin\left[\omega(t-\tau)\right]\mathrm{d}\tau,\ 0\le t<t_0 \\ G(t_0)=\int_0^{t_0} f'(\tau)\cdot\sin\left[\omega(t-\tau)\right]\mathrm{d}\tau,\ t\ge t_0 \end{cases}. \tag{16}$$

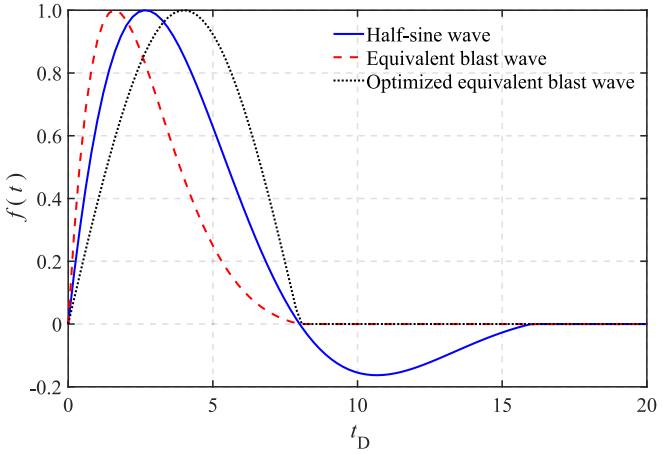

Fig. 2. Three types of blast loading curve.

By combining Eqs. (15) and (16), the transient DSCF for the tunnel can be derived, providing a theoretical evaluation of the tunnel stress state under the influence of near-field blasts. In this study, the elastic parameters for the rock mass used in theoretical calculations are defined as follows: Poisson's ratio $v=0.25$ and density $\rho=2700$ kg/m^3. The P-wave velocity was typically within a range of 4000–5500 m/s and the wave velocity c_p was set at 4500 m/s.

3.3 Transient blast response and analysis

To investigate and analyze the transient response of the tunnel subjected to near-field blast waves, the temporal and spatial distributions of the DSCF under different dimensionless times t_D, tunnel radii a, blast source distances r_0, and Poisson's ratios v were determined. Figure 3 shows the spatial distributions of the DSCF around the tunnel with different wavelengths, tunnel radii, and blast source distances at the peak time of the near-field blast waves. The DSCF was symmetrically distributed around the incident angle $\theta=\pi$. For all conditions, the DSCF reached its minimum value at $\theta=\pi$ and the minimum DSCF value was less than 0, indicating the presence of tensile stress at the incident angle. Owing to the curvature of the cylindrical wave, the maximum DSCF values shifted toward the wave-facing side. The maximum DSCF appeared at $3\pi/5$ and $7\pi/5$, $14\pi/25$ and $36\pi/25$, and $9\pi/17$ and $25\pi/17$ for $r_0=3a$, $5a$ and $10a$, respectively. This indicates that the angles at which the maximum DSCF values occur are $\theta=\pi-\arccos(a/r_0)$ and $\pi+\arccos(a/r_0)$, corresponding to the angles between the tangents formed by the explosion source and circular tunnel. This phenomenon implies that the blast source distance and tunnel radius directly influence the spatial distribution of the DSCF. When the blast source distance was significantly greater than the tunnel radius, the angles at which the maximum DSCF occurred converged to $\pi/2$ and $3\pi/2$. In this scenario, the curvature of the cylindrical wave approached zero and the wave effectively degenerated into a plane wave. In addition, a lower r_0 and a resulted in significant compressive and tensile stress concentrations. The DSCF values gradually decreased as r_0 and a increased, indicating that the energy of the blast stress wave dissipated during propagation, thereby alleviating the dynamic stress concentration in the tunnel. Even at larger r_0 and a, the near-field blasts resulted in significant compressive stress concentrations around the tunnel without causing significant tensile stress concentrations. The spatial distribution characteristics of the DSCF remained the same for different blast wave wavelengths; however, the DSCF values differed, indicating that the blast wave wavelength only affected the magnitude of the DSCF and not its spatial distribution.

Understanding the temporal distribution of the DSCF is crucial for assessing the tunnel stability. As shown in Fig. 4, the DSCF initially increased with t_D at $\theta=0$, reaching its maximum value below 0.55, then rapidly decreased to a minimum value, and finally gradually approached

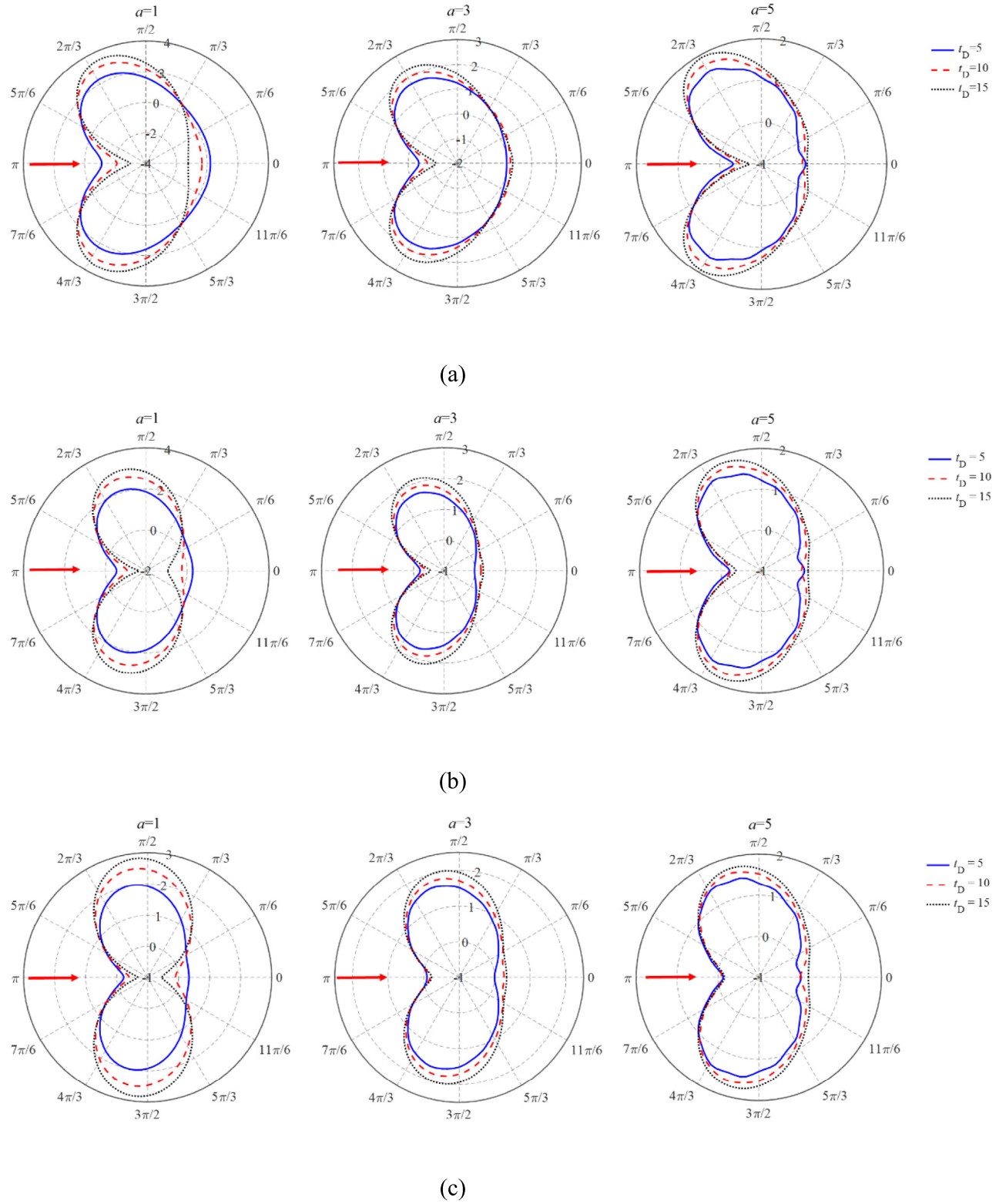

Fig. 3. Spatial distributions of the DSCF values around the tunnel under near-field blasts. (a) $r_0 = 3a$, (b) $r_0 = 5a$, and (c) $r_0 = 10a$.

zero. When $\theta = \pi$, the DSCF rapidly decreased to its minimum value with increasing t_D and then gradually approached zero. A lower r_0 and a resulted in higher absolute DSCF values. For instance, the maximum and minimum DSCF values at $\theta = 0$, π for $a = 1$ and $r_0 = 3a$ were 1.377, −4.3407 and 1.0984, −3.9459, respectively. This indicates significant tensile stress concentrations and mild compressive stress concentrations on both sidewalls

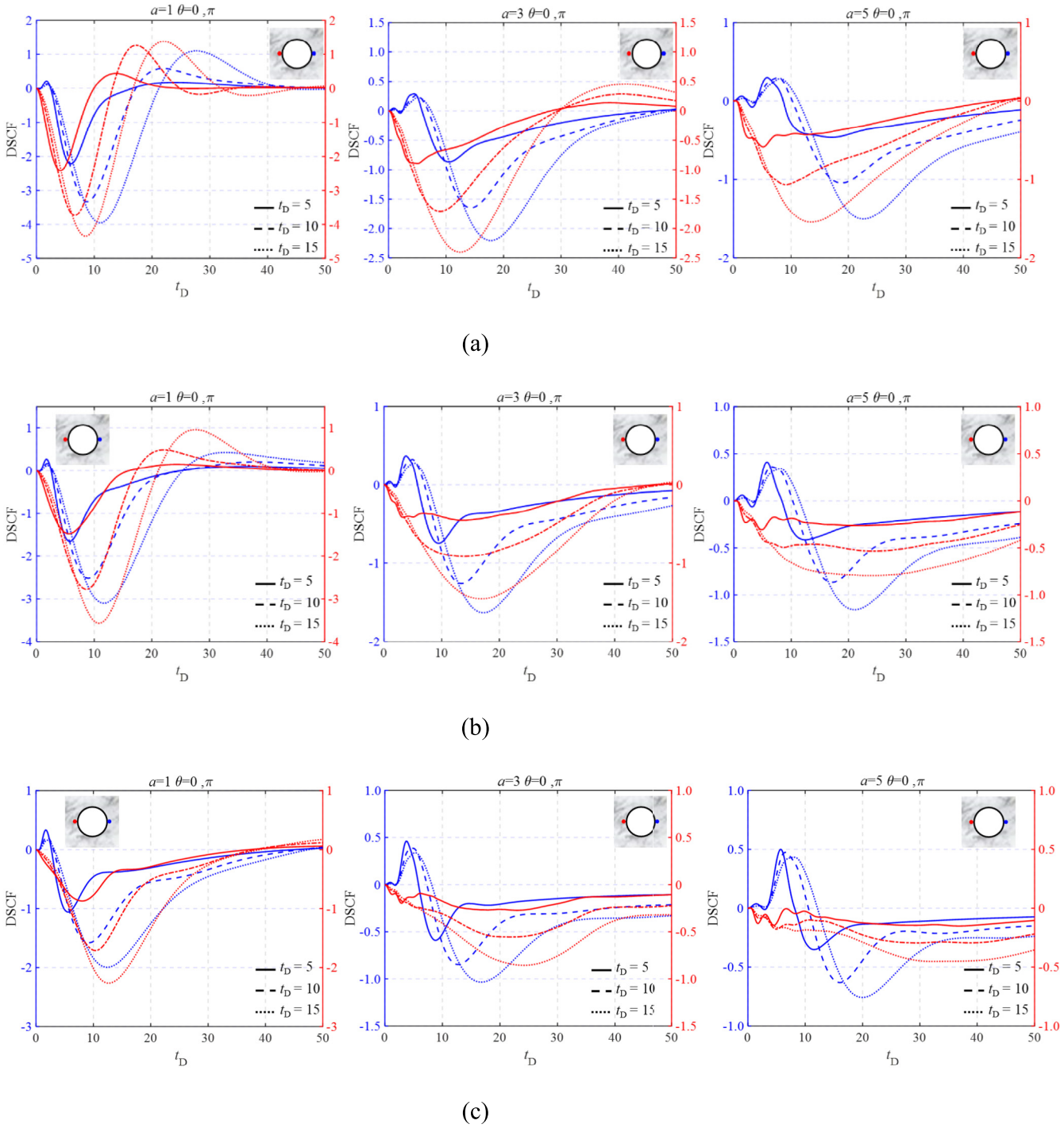

Fig. 4. Temporal distributions of the tensile DSCF values around the tunnel under near-field blasts. (a) $r_0 = 3a$, (b) $r_0 = 5a$, and (c) $r_0 = 10a$.

of the tunnel under near-field blasts. Furthermore, longer blast wave wavelengths increased the absolute DSCF values, making the stress concentrations more pronounced. The absolute DSCF values gradually decreased as r_0 and a increased, thereby reducing the influence of the blast stress waves on the tunnel. Figure 5 shows the temporal distributions of the maximum DSCF around the tunnel under near-field blasts. The DSCF characteristics closely followed the optimized equivalent blast wave pattern. Initially, the DSCF rapidly increased to its maximum value, then slowly decreased to its minimum value, and finally fluctuated toward zero. Notably, the maximum DSCF occurred slightly later than the peak time of the optimized equivalent blast wave. This time lag is mainly due to the time required for the stress wave to propagate to the location of the maximum DSCF and the time required for stress redistribution. The minimum DSCF values were less than zero at $r_0 = 3a$ and $r_0 = 5a$, indicating that the areas

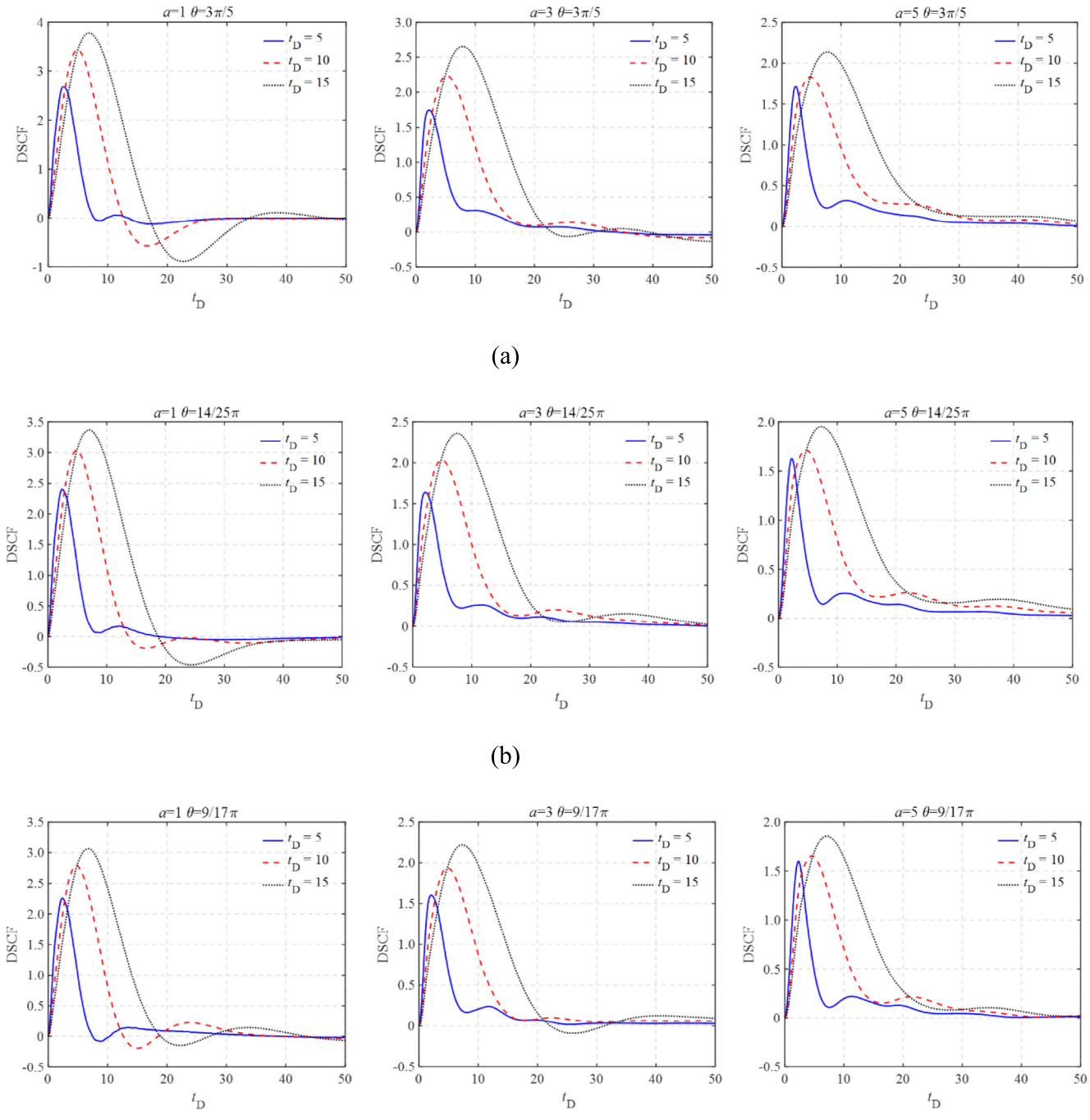

Fig. 5. Temporal distributions of the compressive DSCF values around the tunnel under near-field blasts. (a) $r_0 = 3a$, (b) $r_0 = 5a$, and (c) $r_0 = 10a$.

of compressive stress concentration may also exhibit tensile stresses at certain times. When the compressive stress concentration damages the tunnel surrounding rock, the subsequent weak tensile stress can exacerbate the damage, directly leading to structural failure. In contrast, the minimum DSCF values remained above zero throughout the process at $r_0 = 10a$, indicating that a sufficiently large blast source distance only resulted in compressive stress concentrations without inducing tensile stress. This phenomenon indicates that the blast source distance influences both the DSCF value and sharpness of the DSCF temporal variations. Moreover, the tunnel radius, blast source distance, and blast wave wavelength directly affected the DSCF values. A lower a and r_0 and higher t_D resulted in higher DSCF values. Therefore, the most effective method to mitigate the influence of near-field blasts on existing tunnels is to establish a reasonable separation distance. However, owing to construction requirements and economic consid-

erations, the separation distance between tunnels is often fixed. Reinforcing the surrounding rock in areas of compressive and tensile stress concentrations and appropriately increasing the tunnel radius are more practical for engineering projects.

This study evaluates the effect of tunnel radius a, blast source distance r_0, dimensionless time t_D and Poisson's ratio v on the transient DSCF in detail. Figure 6 shows the effects of these factors on the transient DSCF. In Fig. 6(a), the ranges for v and r_0 were 0.15–0.40 and 3–20, respectively. In Fig. 6(b), the ranges of a and t_D were 1–10 and 5–30, respectively. The wide ranges of these parameters encompass the various working conditions that may occur in the tunnel under near-field blast scenarios. As shown in Fig. 6(a), the absolute maximum and minimum transient DSCF values decreased as v and r_0 increased. For instance, the maximum and minimum DSCF values were 3.4925 and −3.5178, respectively, at $r_0 = 3a$ and $v = 0.15$, whereas the corresponding maximum and minimum DSCF values were 2.1302 and −0.9177, respectively, at $r_0 = 20a$ and $v = 0.4$. This indicates that an increase in r_0 and v mitigate both the compressive and tensile stress concentrations. In addition, the curvature of the r_0-DSCF curve was significantly greater than that of the v-DSCF curve, suggesting that r_0 had a more substantial influence on the DSCF values. Furthermore, changes in r_0 and v did not influence the trends of the DSCF curves and only affected the curvature and DSCF values.

Figure 6(b) shows that the absolute maximum and minimum transient DSCF values decreased as a increased, and increased as t_D increased. This indicates that increasing the tunnel radius can significantly mitigate the dynamic stress

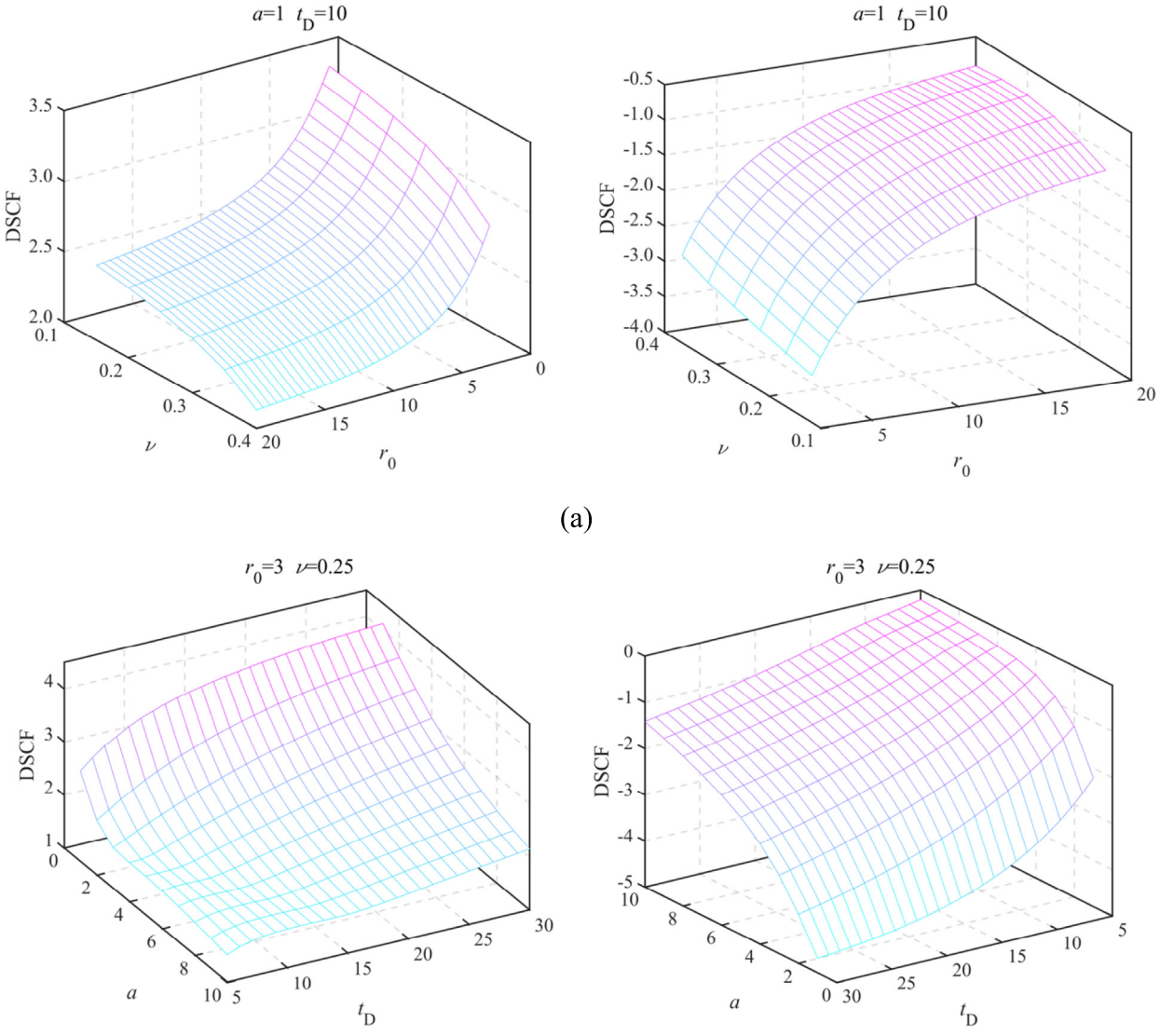

Fig. 6. Variations of the transient DSCF with respect to various influencing factors under near-field blasts. (a) Variations of the transient DSCF with respect to v and r_0, and (b) variations of the transient DSCF with respect to a and t_D.

concentrations. Therefore, in practical engineering applications, increasing the tunnel radius can effectively enhance blast resistance and improve the overall stability of the tunnel. Duhamel's integral is the integral of the steady-state response of a tunnel in the time domain. Longer wavelengths of blast stress waves resulted in extended interaction times with the tunnel, corresponding to lower frequencies and higher DSCF values. Consequently, low-frequency blast waves induced more significant dynamic stress concentrations and were more likely to directly induce structural failure of the tunnel surrounding rock. Moreover, the curvature of the a-DSCF curve was significantly greater than that of the t_D-DSCF curve. This indicates that the tunnel radius has a more substantial influence on the maximum and minimum DSCF values than the blast wave wavelengths, highlighting the importance of considering the tunnel radius in mitigating dynamic stress effects. Furthermore, changes in a and t_D mutually influenced the curvatures of their respective DSCF curves. The curvature of the a-DSCF curve increased with an increase in t_D, whereas the curvature of the t_D-DSCF curve decreased as a increased.

In summary, due to the curvature of the blast stress waves, the maximum DSCF occurred at $\theta = \pi - \arccos(a/r_0)$ and $\pi + \arccos(a/r_0)$, whereas the minimum DSCF occurred at $\theta = \pi$. Both a and r_0 influenced the spatial distribution and values of the DSCF, whereas t_D only affected the DSCF values. The blast stress waves induced compressive stress concentrations near the maximum DSCF locations and induced tensile stress concentrations near the minimum DSCF locations. In some cases, the absolute minimum DSCF values exceeded the absolute maximum DSCF values, indicating that the tensile stress concentrations were more pronounced than the compressive stress concentrations. Because rock is stronger in compression than in tension, the tensile stress concentration areas are more likely to experience tensile failure of the surrounding rock, potentially leading to tunnel instability. The absolute maximum and minimum DSCF values decreased with increasing v, r_0, and a, but increased with increasing t_D. Therefore, in practical engineering applications, selecting surrounding rock with a higher Poisson's ratio, increasing the blast source distance, and enlarging the tunnel radius can effectively mitigate the dynamic stress concentrations. Furthermore, low-frequency blast stress waves are more likely to induce tunnel structural damage, emphasizing the need for careful consideration of the blast wave characteristics in tunnel design and construction.

4 Far-field earthquake model

4.1 Governing equations of the wave field

All types of stress waves can be represented in the cylindrical coordinate system (r, θ) with the tunnel center O as the origin. Thus, the far-field seismic wave can be expressed using the wave function expansion method, as follows (Pao & Mow, 1973):

$$\varphi_E^{(i)} = \varphi_0 e^{i(\alpha x - \omega t)} = \varphi_0 \sum_{n=0}^{\infty} \varepsilon_n (i)^n J_n(\alpha r) \cos(n\theta) e^{-i\omega t}. \tag{17}$$

The scattered P-waves and SV-waves around the tunnel can be written as

$$\varphi_E^{(s)} = \sum_{n=0}^{\infty} A_n^E H_n^{(1)}(\alpha r) \cos(n\theta) e^{-i\omega t}, \tag{18}$$

$$\psi_E^{(s)} = \sum_{n=0}^{\infty} B_n^E H_n^{(1)}(\beta r) \sin(n\theta) e^{-i\omega t}, \tag{19}$$

where A_n^E and B_n^E are the undetermined expansion coefficients.

Therefore, the full wave in the rock mass under plane waves can be expressed as

$$\varphi_E^{(f)} = \sum_{n=0}^{\infty} \left[\varphi_0 \varepsilon_n (i)^n J_n(\alpha r) + A_n^E H_n^{(1)}(\alpha r)\right] \cos(n\theta) e^{-i\omega t}, \tag{20}$$

$$\psi_E^{(f)} = \sum_{n=0}^{\infty} B_n^E H_n^{(1)}(\beta r) \sin(n\theta) e^{-i\omega t}. \tag{21}$$

The expressions for the three types of stress around the tunnel subjected to plane waves are represented as (Tao et al., 2018)

$$\sigma_{rr}^E = \frac{2\mu}{r^2} \sum_{n=0}^{\infty} \left[\varepsilon_n (i)^n \varphi_0 \varepsilon_{11}^{(1)} + A_n^E \varepsilon_{11}^{(3)} + B_n^E \varepsilon_{12}^{(3)}\right] \cos(n\theta) e^{-i\omega t}, \tag{22}$$

$$\sigma_{r\theta}^E = \frac{2\mu}{r^2} \sum_{n=0}^{\infty} \left[\varepsilon_n (i)^n \varphi_0 \varepsilon_{41}^{(1)} + A_n^E \varepsilon_{41}^{(3)} + B_n^E \varepsilon_{42}^{(3)}\right] \sin(n\theta) e^{-i\omega t}, \tag{23}$$

$$\sigma_{\theta\theta}^E = \frac{2\mu}{r^2} \sum_{n=0}^{\infty} \left[\varepsilon_n (i)^n \varphi_0 \varepsilon_{21}^{(1)} + A_n^E \varepsilon_{21}^{(3)} + B_n^E \varepsilon_{22}^{(3)}\right] \cos(n\theta) e^{-i\omega t}. \tag{24}$$

The traction-free condition of the circular tunnel can be expressed as

$$\begin{cases} \sigma_{rr}^E|_{r=a} = 0 \\ \sigma_{r\theta}^E|_{r=a} = 0 \end{cases}. \tag{25}$$

By substituting Eqs. (22) and (23) into Eq. (25), the undetermined expansion coefficients can be derived as follows:

$$A_n^E = -\varepsilon_n (i)^n \varphi_0 \frac{\begin{vmatrix} E_{11}^{(1)} & E_{12}^{(3)} \\ E_{41}^{(1)} & E_{42}^{(3)} \end{vmatrix}}{\begin{vmatrix} E_{11}^{(3)} & E_{12}^{(3)} \\ E_{41}^{(3)} & E_{42}^{(3)} \end{vmatrix}}, \tag{26}$$

$$B_n^{\mathrm{E}} = -\varepsilon_n(\mathrm{i})^n \varphi_0 \frac{\begin{vmatrix} E_{11}^{(3)} & E_{11}^{(1)} \\ E_{41}^{(3)} & E_{41}^{(1)} \end{vmatrix}}{\begin{vmatrix} E_{11}^{(3)} & E_{12}^{(3)} \\ E_{41}^{(3)} & E_{42}^{(3)} \end{vmatrix}}. \tag{27}$$

The maximum radial stress and DSCF resulting from plane P-waves can be expressed as

$$\begin{cases} \sigma_0^{\mathrm{E}} = -\mu\beta^2\varphi_0 \\ \mathrm{DSCF}_{\mathrm{E}} = \frac{\sigma_{\theta\theta}^{\mathrm{E}}}{\sigma_0^{\mathrm{E}}} = -\frac{2}{\beta^2 r^2}\sum_{n=0}^{\infty}\varepsilon_n(\mathrm{i})^n\left[\varepsilon_{21}^{(1)} - A_n^{\mathrm{E}}\varepsilon_{21}^{(3)} - B_n^{\mathrm{E}}\varepsilon_{22}^{(3)}\right]\mathrm{e}^{-\mathrm{i}\omega t}\cos(n\theta) \end{cases}. \tag{28}$$

4.2 Earthquake loading and Fourier transform

Ricker wavelet is extensively employed in seismic modeling and response studies as the preferred source pulse form (Haghighat, 2015; Panji et al., 2022). In this study, the Ricker wavelet was used to simulate the disturbances caused by earthquakes, and the expressions in both the time and frequency domains are provided as follows:

$$\begin{cases} f(t) = \left(1 - \frac{1}{2}\omega_p^2 t^2\right)\mathrm{e}^{-\frac{1}{4}\omega_p^2 t^2} \\ F(\omega) = \frac{4\omega^2\sqrt{\pi}}{\omega_p^3}\mathrm{e}^{\left(-\frac{\omega^2}{\omega_p}\right)} \end{cases}, \tag{29}$$

where ω_p is the main frequency of the Ricker wavelet.

By applying the Fourier transform, the earthquake loading was broken down into a series of simple harmonic waves across various frequencies. Subsequently, an integral transformation was employed to derive the transient DSCF equation that included the time variable t, allowing the determination of the tunnel response at various times under earthquake loading. The transient response can be expressed as (H. Zhao et al., 2023)

$$g(\chi, t) = \frac{1}{\sqrt{2\pi}}\int_{-\infty}^{\infty} F(\omega)\chi(\omega)\mathrm{e}^{-\mathrm{i}\omega t}\mathrm{d}\omega, \tag{30}$$

where $F(\omega)$ is the distribution of the Ricker wavelet in the frequency domain and $\chi(\omega)$ is the steady-state DSCF of the tunnel subjected to plane P-waves.

4.3 Transient earthquake response and analysis

To investigate and analyze the transient response of the underground tunnel subjected to far-field seismic waves, the temporal and spatial distributions of the DSCF values were calculated for various dimensionless times t_{D}, tunnel radii a, and Poisson's ratios v. Figure 7 shows the spatial distributions of the DSCF around the tunnel with different wavelengths and radii at the peak time of the seismic stress waves. Under all conditions, the DSCF initially reached its minimum value at $\theta = 0$ and then gradually increased, reaching its maximum at $\theta = \pi/2$. The transient DSCF exhibited symmetrical distribution around the incident angle $\theta = \pi$, with all of the values remaining positive. This indicates that the peak time of the seismic stress waves only caused compressive stress concentrations. Furthermore, the tunnel radius had a negligible influence on both the distributions and values of the DSCF, underscoring the dominance of other factors affecting the dynamic stress concentrations under specific conditions. The seismic wave wavelength significantly influenced the DSCF values, but only slightly affected the spatial distribution characteristics of the DSCF. As the seismic wave wavelength increased, the DSCF values increased and the spatial distribution exhibited a minor shift. However, the maximum DSCF values still occurred at the incident angles $\theta = 0$, π whereas the minimum DSCF values occurred at the directions perpendicular to the incident angles $\theta = \pi/2$, $3\pi/2$.

Figure 8 shows the temporal distributions of the DSCF values around the tunnel under far-field earthquakes. The DSCF exhibited an oscillatory trend at $\theta = 0$, with two positive and three negative extrema values, showing significant fluctuations as the maximum and minimum values appeared in close succession. Notably, the DSCF values remained relatively low, with the absolute maximum and minimum DSCF values remaining below 0.6 throughout the temporal distributions. This reveals that both compressive and tensile stresses at $\theta = 0$ are minimal, which does not result in significant dynamic stress concentrations. The absolute maximum and minimum DSCF values decreased as the seismic wave wavelength increased. The DSCF followed the pattern of the Ricker wavelet at $\theta = \pi/2$ and the maximum and minimum DSCF values increased with the seismic wave wavelength, which contra-

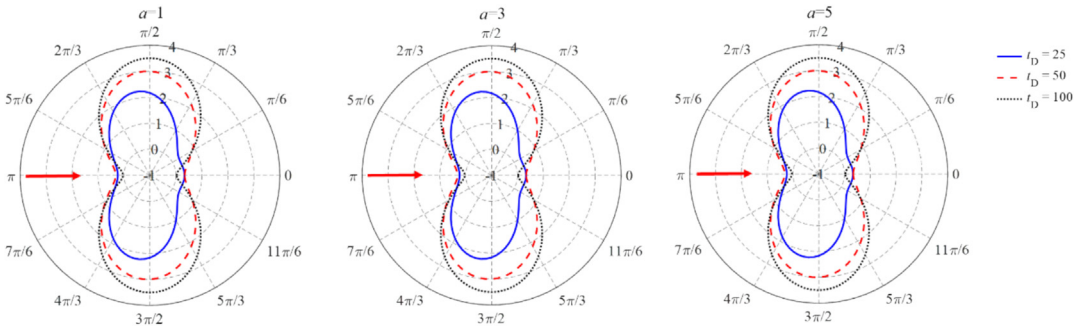

Fig. 7. Spatial distributions of the DSCF values around the tunnel under far-field earthquakes.

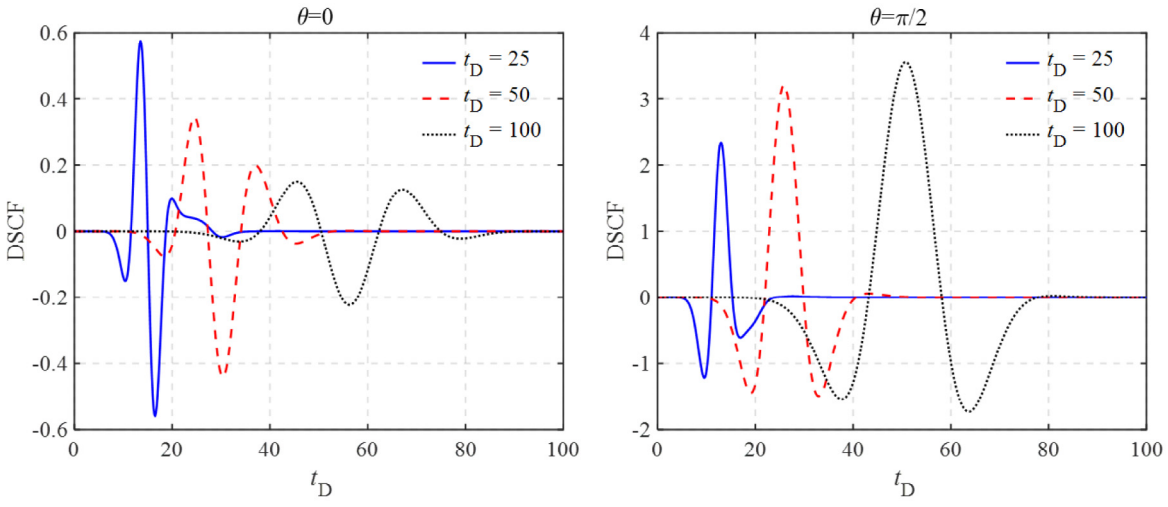

(a)

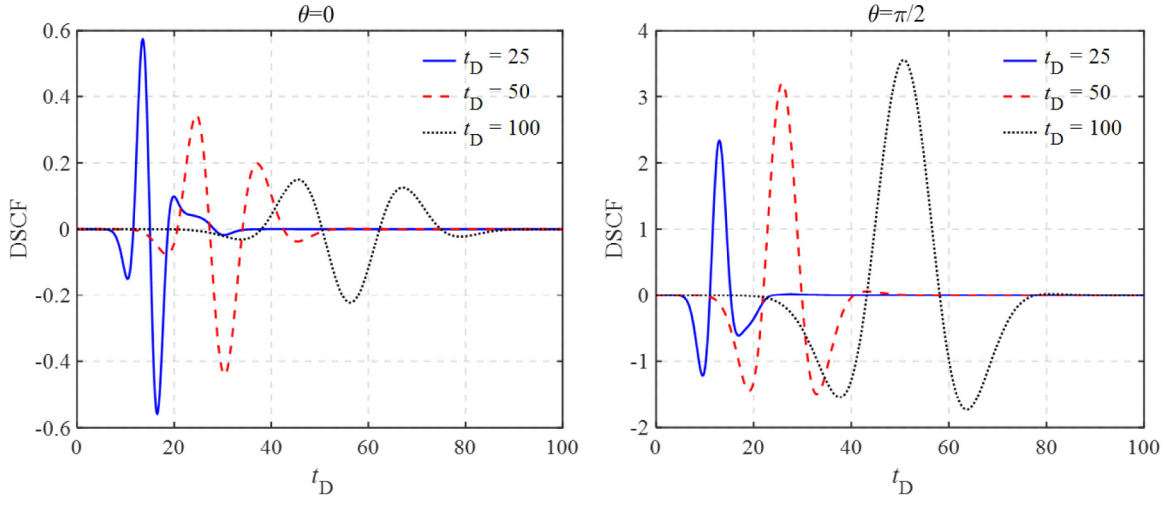

(b)

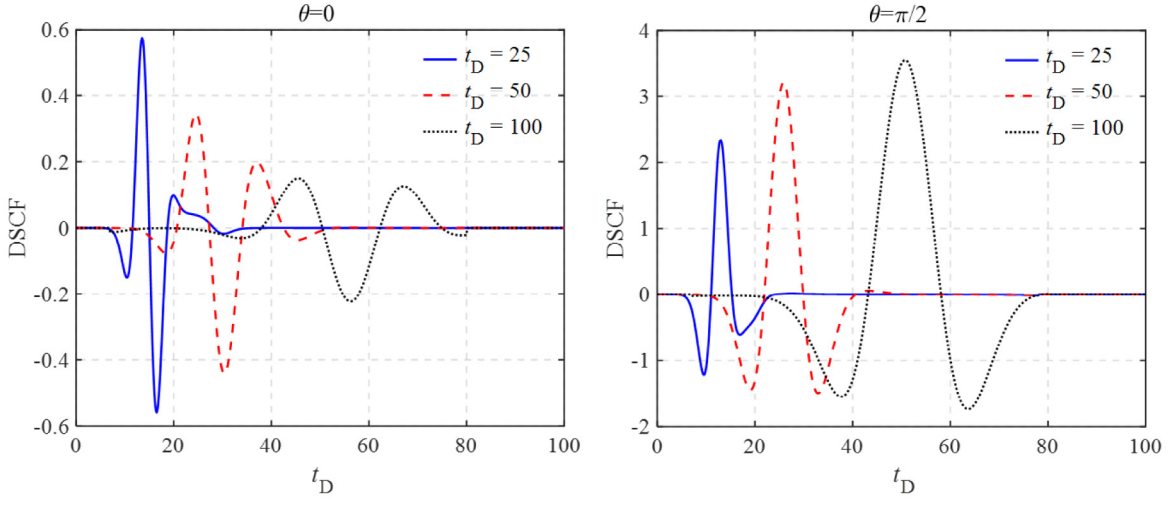

(c)

Fig. 8. Temporal distributions of the DSCF values around the tunnel under far-field earthquakes. (a) $a = 1$, (b) $a = 3$, and (c) $a = 5$.

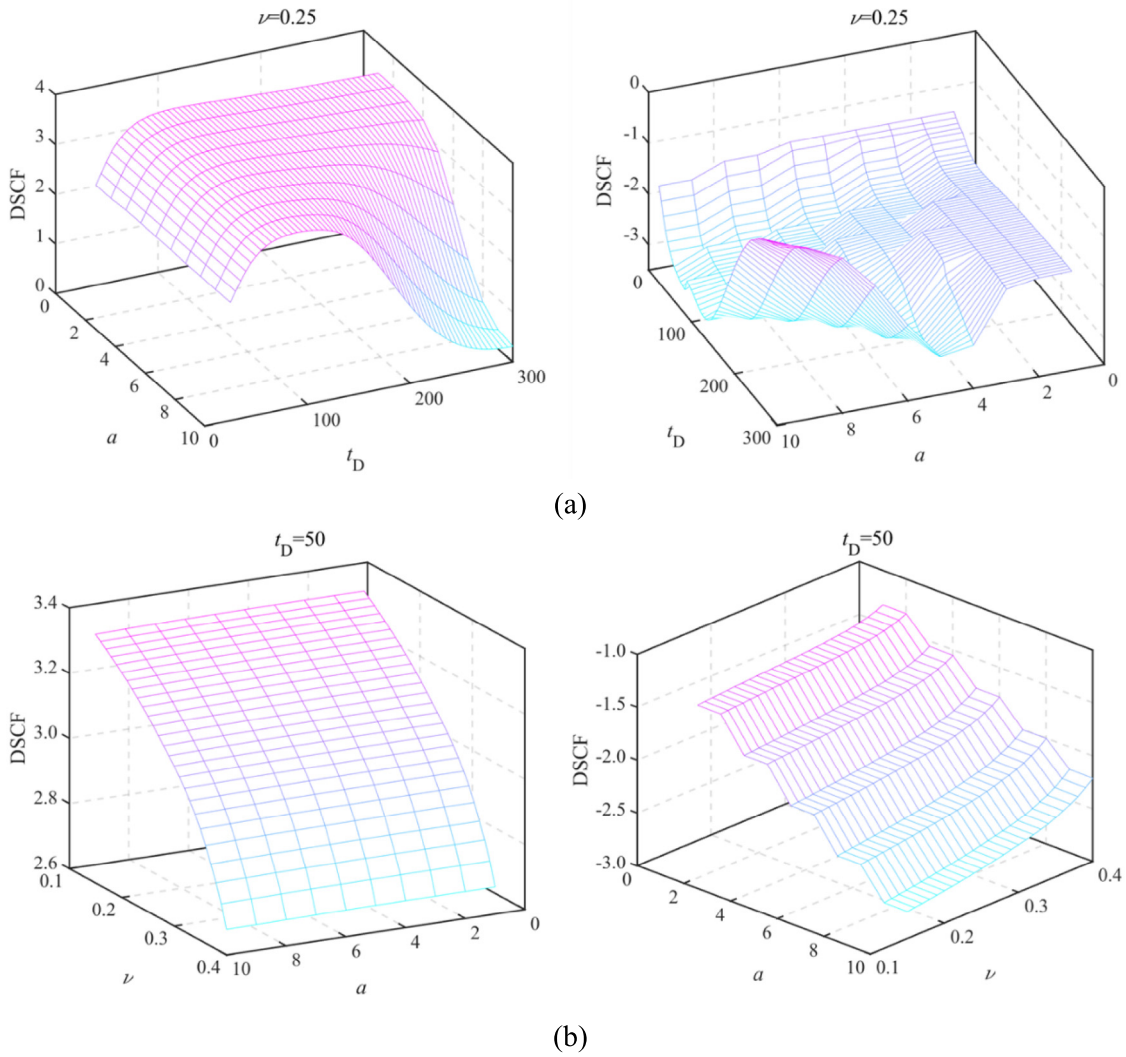

Fig. 9. Variations of the transient DSCF with respect to various influencing factors under far-field earthquakes. (a) Variations of the transient DSCF with respect to a and t_D, and (b) variations of the transient DSCF with respect to a and v.

dicted the DSCF results at $\theta = 0$. This indicates that the surrounding rock at $\theta = \pi/2$ exhibited alternating compressive and tensile stress concentrations. Given that the rock is strong in compression but weak in tension, this alternating stress can easily lead to instability and failure of the tunnel structure.

The three-dimensional curves of the transient DSCF with respect to the tunnel radius, seismic wave wavelength, and Poisson's ratio under far-field earthquakes are shown in Fig. 9. The ranges of the parameters a, v, and t_D were 1–10, 0.15–0.40, and 25–300, respectively. These ranges encompass the various working conditions that may occur in the tunnel under far-field earthquake scenarios. As shown in Fig. 9(a), the maximum transient DSCF initially increased with t_D, reached its maximum value at $t_D = 100$, and then continuously decreased to a constant value. The larger the value of a, the lower the constant DSCF value. When t_D was within a range of 25–110, the DSCF slowly varied with increasing a, with the difference between the DSCF values corresponding to $a = 1$ and 10 being less than 0.1. When t_D was within a range of 110–300, the DSCF decreased as a increased, where higher values of t_D led to a faster reduction in the maximum DSCF. The behavior of the minimum transient DSCF with t_D was dependent on a and showed a complex trend. When a was within a range of 1–5, the minimum DSCF initially decreased with increasing t_D until it reached a minimum value, and then increased before gradually decreasing to a constant value. When a was within a range of 6–10, the initial trend was similar to that when a was within a range of 1–5. However, after the DSCF reached a constant value, the DSCF sharply increased, with the rate of increase being faster for larger values of a. The behavior of the minimum transient DSCF with respect to a was influenced by t_D. When t_D was within a range of 10–140, the DSCF gradually decreased with increasing a, and the rate of decrease became faster as t_D increased. However, when t_D was within a range of 140–300, the DSCF initially decreased

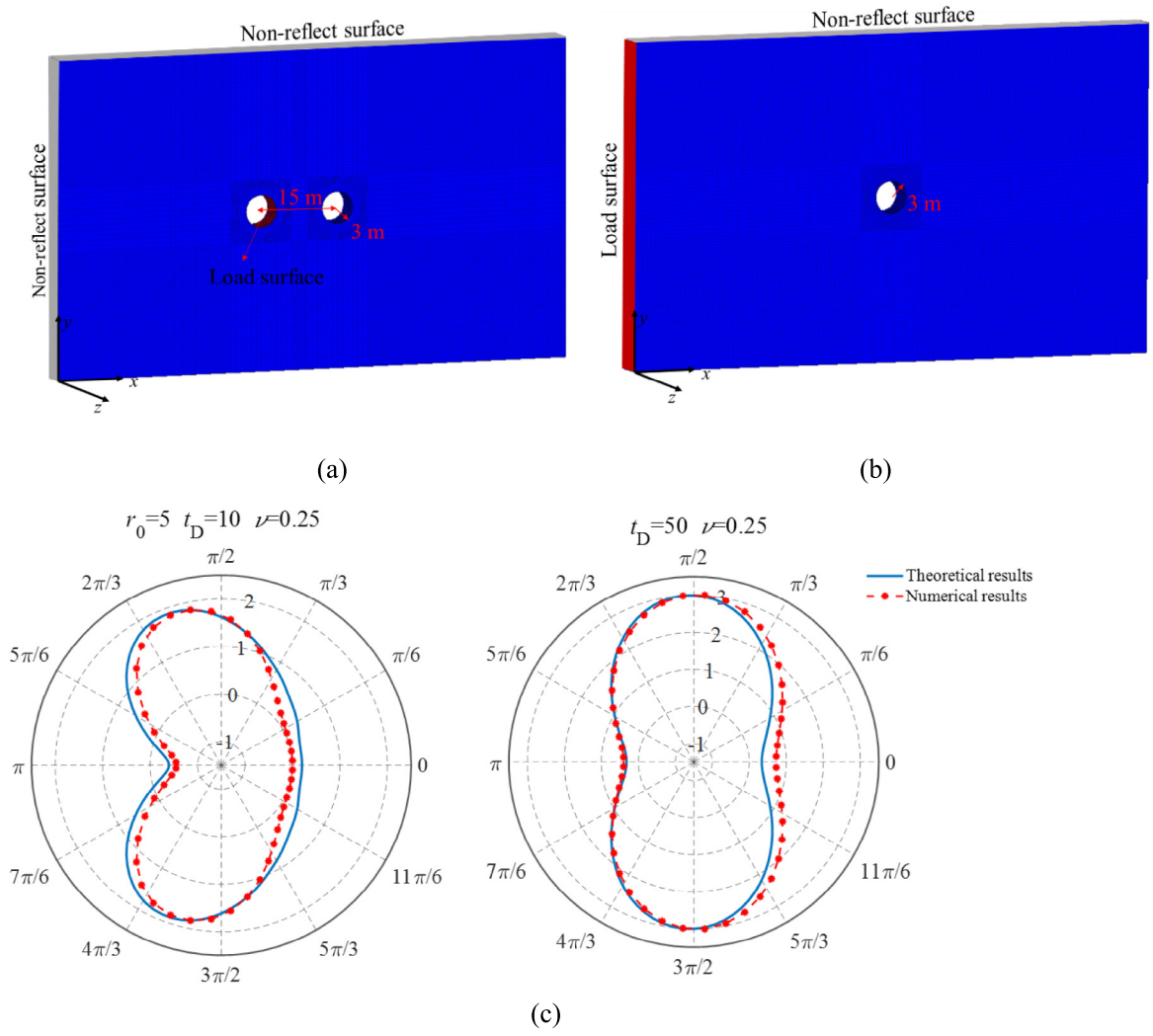

Fig. 10. FEM numerical models and comparison between the theoretical and numerical simulation results. (a) Near-field blast numerical model, (b) far-field earthquake numerical model, and (c) comparison between the theoretical and numerical simulation results.

to a minimum value with increasing a, and then rapidly increased, where the rate of increase accelerated as t_D increased. These observations indicate that changes in a and t_D mutually influence the curvatures of their corresponding DSCF curves. Figure 9(b) shows that the maximum DSCF decreased with increasing ν, and remained relatively invariant with increasing a. The difference between the DSCF values corresponding to $a = 1$ and 10 was less than 0.01. Changes in ν and a did not influence the trend and curvature of their respective DSCF curves. In addition, the minimum DSCF increased with increasing ν and significantly decreased with increasing a, exhibiting an opposite trend to the maximum DSCF. Changes in ν and a did not affect the trends of their respective DSCF curves; however, they influenced the curvature and DSCF values. The 3D plots revealed that increasing the Poisson's ratio of the tunnel surrounding rock significantly reduced the compressive and tensile stress concentrations. The effect of tunnel radius on the DSCF was complex and primarily controlled by both ν and t_D. Moreover, when t_D was within a range of 100–140, the seismic wave wavelength resulted in larger absolute DSCF values, indicating that this wavelength range may be close to the natural frequency of the tunnel, causing structural resonance and significant stress concentrations.

In summary, due to the curvature of the plane wave being zero, the maximum DSCF values occurred at directions perpendicular to the incident angles $\theta = \pi/2$ and $3\pi/2$, whereas the minimum DSCF values appeared at the incident angle $\theta = \pi$. The parameters a and t_D had minimal influence on the distribution characteristics of the DSCF. However, a slightly affected the DSCF values, whereas t_D had a significant influence. Seismic stress waves caused notable compressive and tensile stress concentrations near the directions perpendicular to the incident angles $\theta = \pi/2$ and $3\pi/2$. The absolute DSCF values remained below 1 at the incident angle $\theta = \pi$, indicating that there were no dynamic stress concentrations in this area. Under various conditions, the maximum DSCF values were 2–3 times greater than the absolute minimum

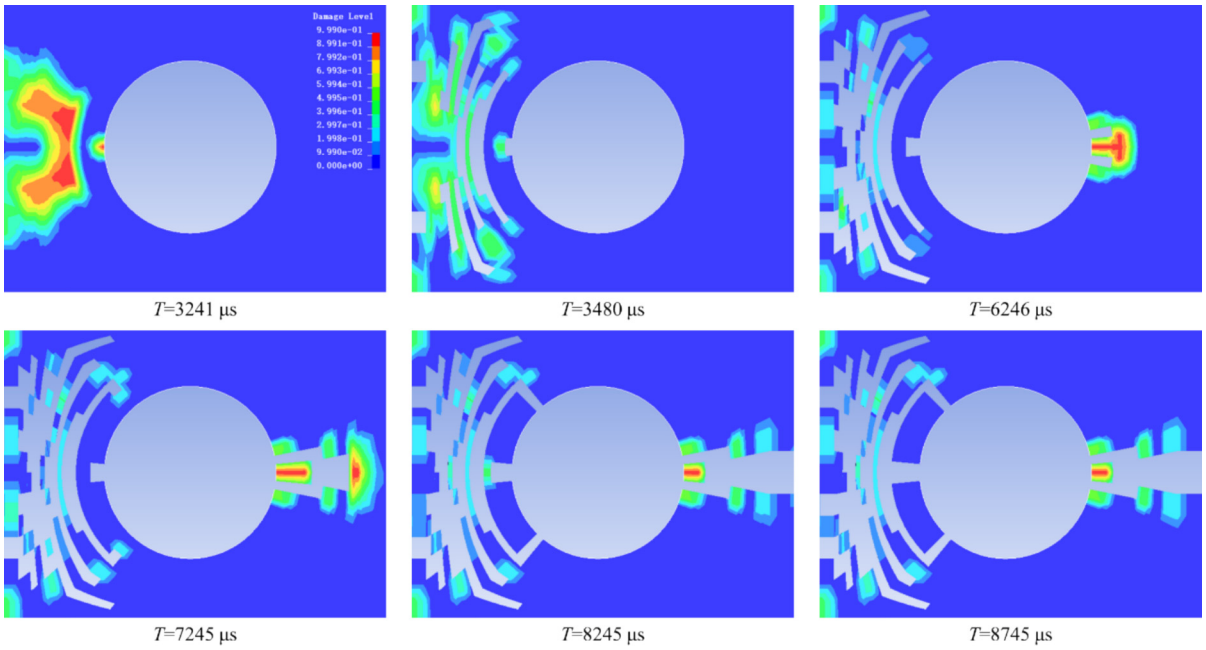

Fig. 11. Damage evolution process of the tunnel surrounding rock under near-field blasts.

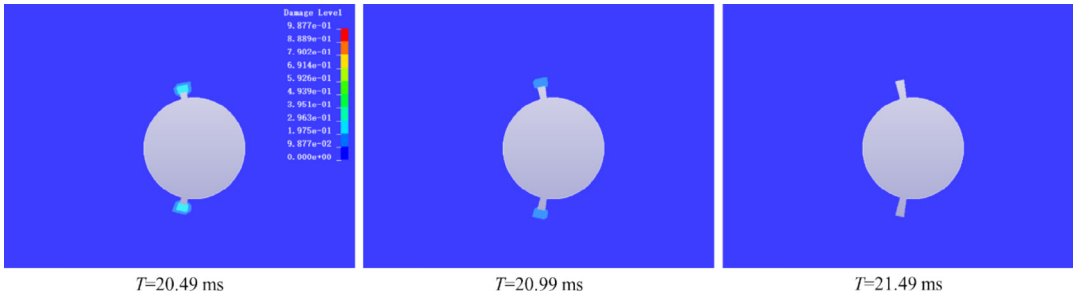

Fig. 12. Damage evolution process of the tunnel surrounding rock under far-field earthquakes.

DSCF values, indicating that the tunnel roof and floor were more prone to shear failure under seismic wave incidence, leading to tunnel instability. The complex variations of the maximum and minimum DSCF values with v, a, and t_D indicate that it is crucial to consider these parameters in engineering practice. It is advisable to select surrounding rock with a higher Poisson's ratio and design seismic-resistant structures based on specific conditions. Furthermore, selecting an appropriate tunnel radius and reinforcing the tunnel roof and floor can mitigate the stress concentrations induced by seismic waves close to the natural frequency of the tunnel.

5 Validation and numerical simulation analysis

5.1 Validation method

To validate the theoretical results, numerical simulations were conducted using ANSYS LS-DYNA FEM software. Given that most tunnels in actual engineering applications have a medium cross-section, the tunnel radius was set at 3 m and the model dimensions were 100 m × 60 m × 5 m, as shown in Fig. 10. In the near-field blast numerical model, the distance between the two tunnels was 15 m, corresponding to $r_0 = 5a$. The optimized equivalent blast wave was applied to the left tunnel wall, generating a cylindrical P-wave that propagated toward the right side of the tunnel. To prevent boundary effects and reflections from affecting the numerical simulation results, all six surfaces of the numerical model were set as non-reflective boundaries. For the far-field earthquake numerical model, the Ricker wavelet was applied to the left surface. Similarly, the other five surfaces of the numerical model were set as non-reflective boundaries. In addition, the dimensionless times t_D for the equivalent blast wave and Ricker wavelet were set at 10 and 50, respectively, with a stress amplitude of 60 MPa. The rock mass was modeled as an elastic material with a density ρ of 2700 kg/m3, Poisson's ratio v of 0.25, and wave velocity c_p of 4500 m/s. Comparison between the theoretical and numerical simulation results is shown in Fig. 10(c). The results demonstrated good consistency in the spatial distribution and values of

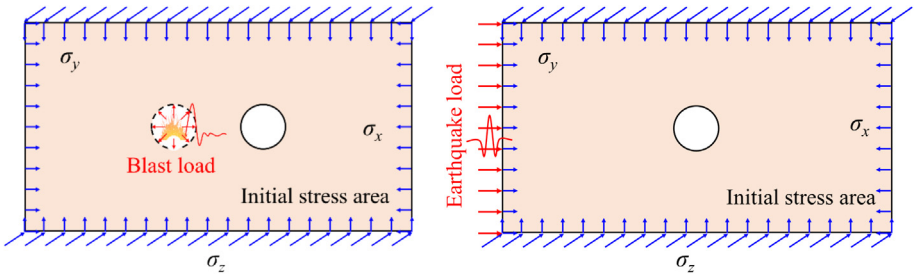

Fig. 13. Numerical model with coupled static–dynamic loading.

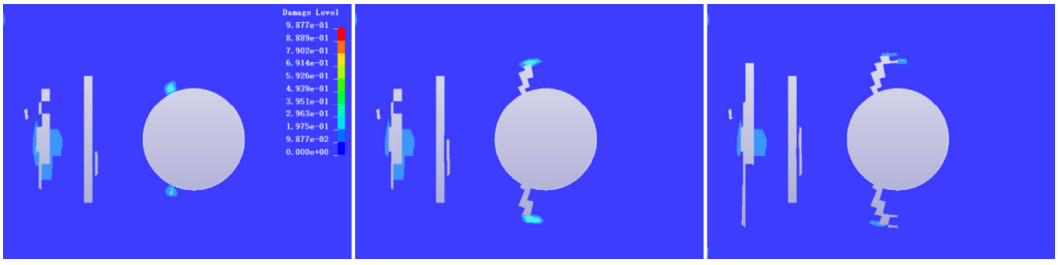

(a)

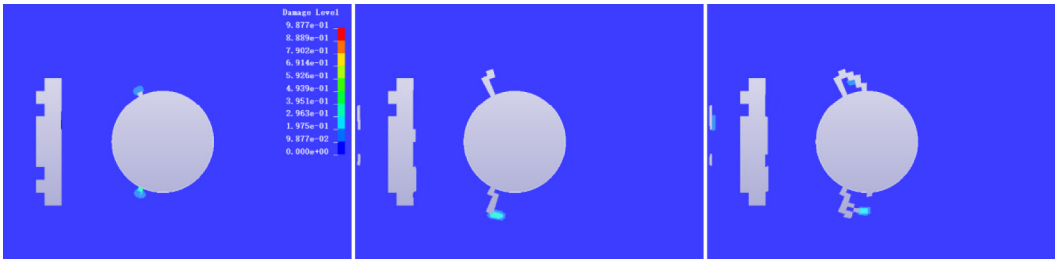

(b)

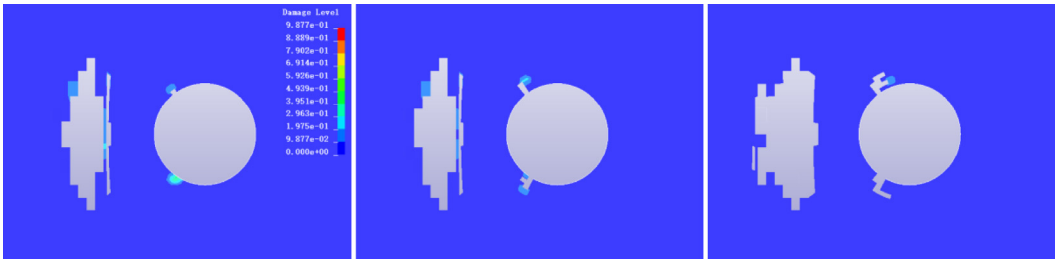

(c)

Fig. 14. Deformation and damage evolution of the deep-buried tunnel subjected to initial stress under near-field blasts. (a) $\gamma = 0.5$, (b) $\gamma = 1.0$, and (c) $\gamma = 1.5$.

the DSCF under both transient disturbances, validating the effectiveness of the derivation process and the theoretical results. However, some discrepancies in details may arise because the basic elements of the numerical model are cuboidal, which causes the tunnel boundary composed of these finite elements to differ slightly from a true circular boundary. To minimize the computational time and ensure accuracy of the numerical simulation results, the size of the element in the plane was selected as 0.25 m × 0.25 m.

5.2 Damage characteristics of the underground tunnel

Various materials have been used to model rock mechanical behavior in numerical simulations to understand its failure characteristics, such as the Riedel–Hiermaier–Thoma (RHT) model, Holmquist–Johnso–Cook (HJC) model, and continuous surface cap model (CSCM) (Hong et al., 2022; Li et al., 2023). The CSCM is widely applied in dynamic failure simulations of hard rock, encompassing

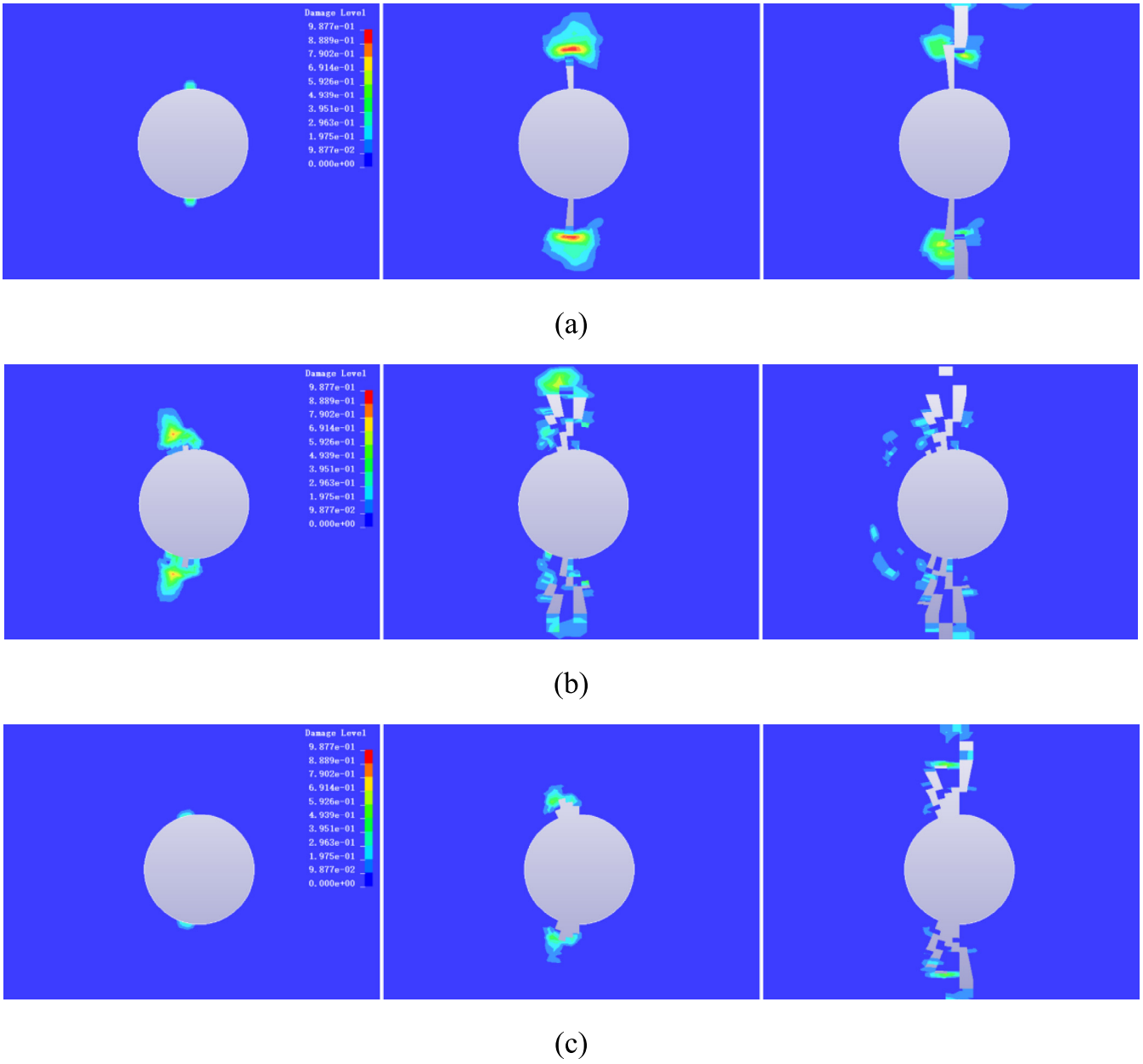

Fig. 15. Deformation and damage evolution of the deep-buried tunnel subjected to initial stress under far-field earthquakes. (a) $\gamma = 0.5$, (b) $\gamma = 1.0$, and (c) $\gamma = 1.5$.

compression, tension, and shear failures, and effectively represents the strain rate effects of the rock. Hence, CSCM for transient disturbances was employed in this study to evaluate the tunnel damage characteristics and failure modes under two typical disturbances. The basic parameters of the CSCM were set to be consistent with those of an elastic material, and the loading stress amplitude σ_d was increased to 150 MPa.

The damage evolution process of the tunnel surrounding rock under near-field blasts is illustrated in Fig. 11. As the cylindrical P-wave propagated to the left sidewall of the tunnel, it caused spalling damage to the rock mass on the blast-facing side, leading to tensile damage of the left sidewall. When the blast stress wave reached the right sidewall of the tunnel, it induced tensile failure in the surrounding rock. Subsequently, the scattering wave exacerbated the spalling damage on the rock mass and tensile damage on the right sidewall, with the number of deleted elements gradually increasing. Meanwhile, shear failure occurred in the surrounding rock at $\theta = 3\pi/4$ and $5\pi/4$. The tensile and shear failure areas on the left sidewall eventually coalesced with the spalling areas, whereas those on the right sidewall exhibited significant tensile failure. The failure modes of the surrounding rock were determined by analyzing the stress states of the deleted elements. Throughout the near-field blast process, the damage range of the tunnel sur-

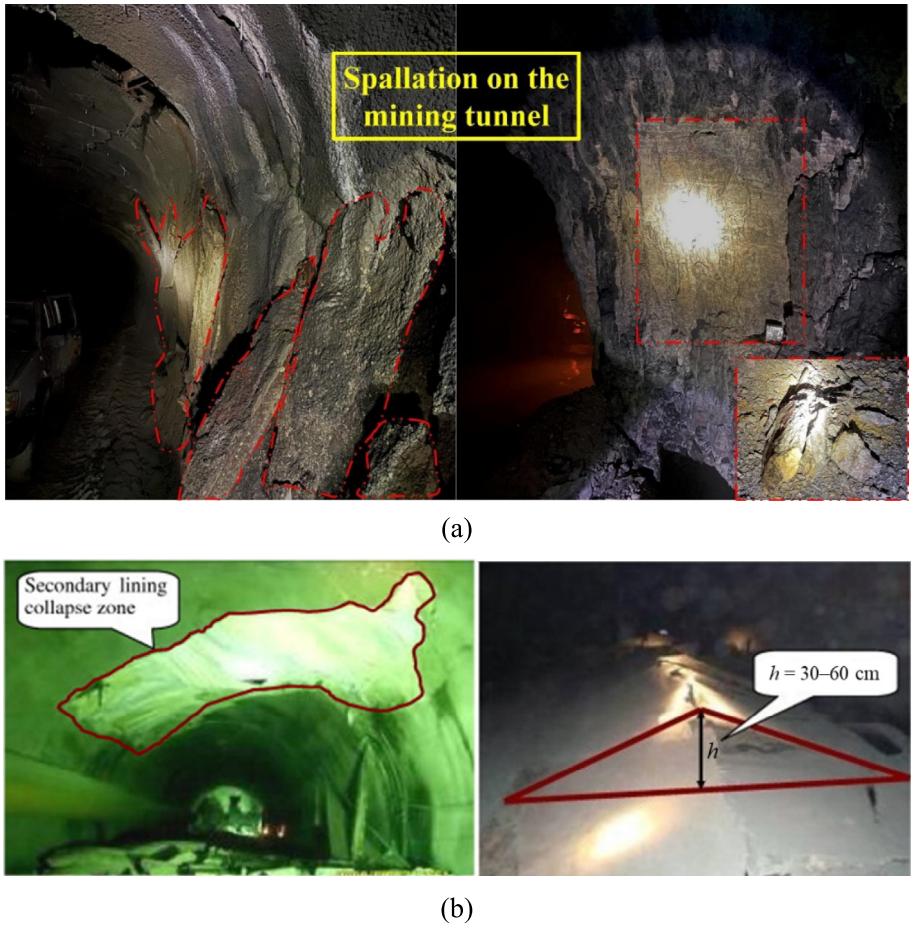

Fig. 16. Damage characteristics of tunnels in actual engineering projects. (a) Spallation of tunnel side in Kaiyang phosphate mine under near-field blasts (R. Zhao et al., 2023), and (b) roof collapse and floor uplift of tunnels after Wenchuan earthquake (Shen et al., 2014).

rounding rock closely matched the theoretical stress concentration areas. However, there were some discrepancies in the results. In particular, the shear failure area in the numerical simulation results showed a greater deflection toward the blast-facing side compared with that in the theoretical results. This discrepancy is primarily due to the internal spalling damage within the rock on the blast-facing side.

Figure 12 illustrates the damage evolution process of tunnel surrounding rock under far-field earthquakes. As the plane P-wave propagated through the tunnel, it caused tensile failure in the surrounding rock at directions perpendicular to the incident angles. With continuous propagation of the stress wave, the damage to the tunnel roof and floor gradually increased. During far-field seismic loading, the range of damage to the tunnel surrounding rock closely matched the theoretical stress concentration areas. Analysis of the stress states of the deleted elements revealed that although the compressive stress concentrations were significantly greater than the tensile stress concentrations (as indicated by the theoretical results), the actual failure of the tunnel surrounding rock was primarily induced by the tensile stress concentrations, highlighting the inherent weakness of the rock under tension.

To investigate the effect of initial stress on the damage characteristics of deep-buried tunnels, the initial stress was loaded into the numerical model described in the previous section. The loading method for the coupled static–dynamic stress is illustrated in Fig. 13. The initial stresses were loaded along the positive direction of the x , y, and z axes. The initial stress along the tunnel axial σ_z was set to a constant value of 15 MPa, whereas the initial stresses in the other two directions were controlled by the lateral pressure coefficient γ, defined as the ratio of σ_x and σ_y. In this study, γ was set at 0.5, 1.0, and 1.5, corresponding to the following coupled static–dynamic stress states:

(1) $\gamma = 0.5$, $\sigma_x = 15$ MPa, $\sigma_y = 30$ MPa, $\sigma_z = 15$ MPa, $\sigma_d = 150$ MPa;
(2) $\gamma = 1.0$, $\sigma_x = 30$ MPa, $\sigma_y = 30$ MPa, $\sigma_z = 15$ MPa, $\sigma_d = 150$ MPa;
(3) $\gamma = 1.5$, $\sigma_x = 45$ MPa, $\sigma_y = 30$ MPa, $\sigma_z = 15$ MPa, $\sigma_d = 150$ MPa.

The Dynain method was employed to apply various coupled static–dynamic stresses to a deep-buried tunnel

model, utilizing coupled implicit–explicit analysis to determine the tunnel damage characteristics. Figure 14 illustrates the damage evolution process of the deep-buried tunnel under near-field blasts. Under the initial stress, the spalling damage on the blast-facing side was suppressed, and the damage range was smaller than that of the tunnel model without initial stress. Shear failure occurred in two compressive stress concentration areas on the left sidewall, and the severity of the shear failure was more pronounced. Meanwhile, no tensile failure was observed on either sidewalls of the tunnel, indicating that the initial stress suppressed the tensile failure while exacerbating the shear failure. This phenomenon was consistent with the findings of Li and Weng (2016). Furthermore, as the initial lateral pressure coefficient γ increased, the spalling damage range increased, whereas the shear damage on the left sidewall decreased. This is because a higher lateral pressure coefficient γ results in higher strain energy in the rock mass. Under transient disturbances, the combined effect of the transient loading and initial stress unloading led to more severe rock failure and a larger damage range. Most of the transient disturbance energy was used for spalling damage, reducing the energy acting on the surrounding rock, and alleviating shear damage on the left sidewall of the tunnel. Figure 15 shows the damage evolution process of the deep-buried tunnel under far-field earthquakes. Significant damage occurred at the tunnel roof and floor under the initial stress, which was consistent with the damage characteristics of the tunnel without initial stress, but to a significantly larger range. As the lateral pressure coefficient γ increased, the damage range of the tunnel roof and floor also increased, indicating that initial stress significantly exacerbated structural damage in deep-buried tunnels subjected to far-field seismic waves. During the damage evolution process induced by the seismic disturbances, the transient loading and initial stress unloading acted simultaneously on these areas. With a constant seismic load, a higher lateral pressure coefficient γ resulted in the surrounding rock releasing more strain energy, leading to more severe damage to the tunnel roof and floor.

6 Discussion

In this study, the wave function expansion method provided direct analytical solutions that were more accurate than the numerical solutions obtained using the complex variable function method. The truncation order N of the Bessel function was greater than 10, which effectively ensured the accuracy of the theoretical results. Furthermore, few researchers have been devoted to analyzing the transient response differences of tunnels under various disturbances. Based on a comparison of the theoretical results in the elastic stage, the differences in the spatiotemporal distribution characteristics of the transient DSCF under blast and seismic disturbances can be summarized as follows:

(1) At the peak time of the disturbance load, the locations of the maximum DSCF values differed, whereas the locations of the minimum DSCF values remained the same. The maximum DSCF values occurred at $\theta = \pi - \arccos(a/r_0)$ and $\pi + \arccos(a/r_0)$ under near-field blasts, whereas under far-field earthquakes, the maximum DSCF values occurred at $\theta = \pi/2$ and $3\pi/2$. The minimum DSCF values were consistently observed at the incident angles $\theta = \pi$ and 0. However, when r_0/a approached infinity, the cylindrical wave approximated a plane wave, causing the maximum DSCF values to appear at $\theta = \pi/2$ and $3\pi/2$ under blast stress waves. In addition, the blast stress waves caused both compressive and tensile stress concentrations, whereas seismic stress waves induced only compressive stress concentrations.
(2) The areas of compressive and tensile stress concentrations differed for cylindrical waves; however, they were the same for plane waves, indicating that stress variations were more intense in the stress concentration areas of plane waves. For cylindrical waves, the absolute minimum DSCF values were greater than the absolute maximum DSCF values, whereas for plane waves, the maximum DSCF values were significantly greater than the absolute minimum DSCF values. This indicates that the tunnel instability under near-field blasts is primarily due to tensile failure on the tunnel sidewalls, whereas it is primarily due to the failure of the tunnel roof and floor under far-field earthquakes.
(3) For near-field blasts, the absolute maximum and minimum DSCF values decreased with increasing v, r_0, and a; however, they increased with increasing t_D. However, under far-field earthquakes, the variations of the absolute maximum and minimum DSCF values with v, a, and t_D were more complex. Even though the variations of the DSCF values with v under far-field earthquakes were similar to those under near-field blasts, the variations of the DSCF values with a and t_D showed distinct differences.

By comparing the numerical simulation results in the plastic stage, the differences in the damage characteristics of the tunnel with initial stress under blast and seismic disturbances are as follows:

(1) Without initial stress, near-field blast waves caused extensive spalling damage to the rock mass on the blast-facing side. In addition, two areas of shear damage occurred on the left sidewall, and tensile damage appeared on both sides of the surrounding rock. In contrast, under far-field earthquakes, tensile damage occurred only at the tunnel roof and floor. The damage areas under both transient disturbances closely matched the dynamic stress concentration areas obtained from the theoretical calculations.

(2) Under initial stress, the damaged area of the deep-buried tunnel subjected to near-field blast waves differed from that without initial stress, whereas the damaged area under far-field earthquakes remained consistent with and without initial stress. For near-field blasts, the spalling damage to the rock mass was reduced, with only two shear-damaged areas on the left sidewall and no tensile damage on the tunnel sides. Structural failure occurred only at the tunnel roof and floor under far-field earthquakes.
(3) The lateral pressure coefficient γ affected the damage characteristics of the deep-buried tunnel differently under near-field blasts and far-field earthquakes. For near-field blasts, the spalling-damaged area increased with the lateral pressure coefficient γ, whereas the shear-damaged area decreased. In contrast, the damage range at the tunnel roof and floor increased with the lateral pressure coefficient γ under far-field earthquakes.

Comparison of the theoretical and numerical simulation results revealed that the differences in the dynamic stress concentration distribution and damage characteristics between near-field blasts and far-field earthquakes were primarily due to the combined effects of the stress wave curvature and transient load waveform. The damaged area for near-field blast stress waves was primarily concentrated on the blast-facing side of the surrounding rock, whereas the damaged area was primarily at the tunnel roof and floor for far-field earthquakes. This is consistent with the tunnel failure characteristics observed in practical engineering applications (Shen et al., 2014; R. Zhao et al., 2023), as shown in Fig. 16. Therefore, this study provides both theoretical and numerical references for the blast and earthquake resistant designs of tunnels. In tunnel design, special attention should be given to the dynamic stress concentration areas, and reinforcement efforts should be focused on areas prone to damage.

7 Conclusions

The differences in the dynamic response and damage characteristics of underground tunnel under near-field blasts and far-field earthquakes were analyzed in detail in this study. Through theoretical calculations and numerical simulations, the spatiotemporal distribution characteristics of the DSCF and failure mechanisms of the tunnel were obtained. The effects of the tunnel radius, blast source distance, transient disturbance wavelength, Poisson's ratio, and initial stress on the transient response of the tunnel were evaluated. The results indicated that the differences in the dynamic response of the underground tunnel were primarily due to the curvature of the stress waves and the transient load waveform. The maximum DSCF value occurred at $\theta = \pi - \arccos(a/r_0)$ and $\pi + \arccos(a/r_0)$ under near-field blasts, whereas the maximum DSCF value occurred at $\theta = \pi/2$ and $3\pi/2$ under far-field earthquakes. In both cases, the minimum DSCF value occurred at the incident angles $\theta = \pi$ and 0. The tunnel exhibited compressive stress concentrations at locations of the maximum DSCF and tensile stress concentrations at locations of the minimum DSCF. Conversely, the seismic stress waves resulted in both compressive and tensile stress concentrations at the maximum DSCF located at the tunnel roof and floor. The initial stress suppressed the tensile damage and enhanced the shear damage in the surrounding rock. Therefore, under initial stress, the blast stress waves did not cause tensile damage on the left and right sidewalls of the tunnel, but led to spalling damage of the rock mass on the blast-facing side and shear damage on the left sidewall. Structural failure occurred only at the tunnel roof and floor under far-field earthquakes. Furthermore, as the lateral pressure coefficient γ increased, the range of spalling-damaged area increased, whereas the range of shear failure area decreased under near-field blasts. For far-field earthquakes, the damage range at the tunnel roof and floor increased with the lateral pressure coefficient γ.

This study facilitates the theoretical and numerical analyses of the failure mechanisms and structural support of deep-buried tunnels subjected to blast and seismic stress waves, offering significant engineering implications for disaster prevention in deep geotechnical engineering.

Data availability

The data that support the findings of this study are available from the corresponding author upon reasonable request.

CRediT authorship contribution statement

Hao Luo: Writing – review & editing, Writing – original draft, Software, Methodology. **Ming Tao:** Supervision, Funding acquisition, Conceptualization. **Zhixian Hong:** Software, Investigation. **Gongliang Xiang:** Data curation. **Chengqing Wu:** Validation, Supervision.

Declaration of competing interest

The authors declare that they have no known competing financial interests or personal relationships that could have appeared to influence the work reported in this paper.

Acknowledgment

The research presented in this paper was supported by the National Natural Science Foundation of China (Grant Nos. 52334003 and 52274105) and the Fundamental Research Funds for the Central Universities of Central South University (Grant No. CX20240263).

Appendix

$$\varepsilon_{11}^{1} = \left(n^2 + n - \frac{\beta^2 r^2}{2}\right) J_n(\alpha r) - \alpha r J_{n-1}(\alpha r)$$

$$\varepsilon_{11}^{3} = \left(n^2 + n - \frac{\beta^2 r^2}{2}\right) H_n^{(1)}(\alpha r) - \alpha r H_{n-1}^{(1)}(\alpha r)$$

$$\varepsilon_{12}^{3} = n\left[-(n+1)H_n^{(1)}(\beta r) + \beta r H_{n-1}^{(1)}(\beta r)\right]$$

$$\varepsilon_{21}^{1} = -\left(n^2 + n + \frac{\beta^2 r^2}{2} - \alpha^2 r^2\right) J_n(\alpha r) + \alpha r J_{n-1}(\alpha r)$$

$$\varepsilon_{21}^{3} = -\left(n^2 + n + \frac{\beta^2 r^2}{2} - \alpha^2 r^2\right) H_n^{(1)}(\alpha r) + \alpha r H_{n-1}^{(1)}(\alpha r)$$

$$\varepsilon_{22}^{3} = n\left[(n+1)H_n^{(1)}(\beta r) - \beta r H_{n-1}^{(1)}(\beta r)\right]$$

$$\varepsilon_{41}^{1} = -n[-(n+1)J_n(\alpha r) + \alpha r J_{n-1}(\alpha r)]$$

$$\varepsilon_{41}^{3} = -n\left[-(n+1)H_n^{(1)}(\alpha r) + \alpha r H_{n-1}^{(1)}(\alpha r)\right]$$

$$\varepsilon_{42}^{3} = -\left(n^2 + n - \frac{\beta^2 r^2}{2}\right) H_n^{(1)}(\beta r) + \beta r H_{n-1}^{(1)}(\beta r)$$

References

Callisto, L., & Ricci, C. (2019). Interpretation and back-analysis of the damage observed in a deep tunnel after the 2016 Norcia earthquake in Italy. *Tunnelling and Underground Space Technology, 89*, 238–248.

Elgamal, A., & Elfaris, N. (2022). Adverse impact of earthquake seismic loading on angular offset tunnels and effects of isolation grout. *Infrastructures, 7*(7), 87.

Gu, H. L., Lai, X. P., Tao, M., Momeni, A., & Zhang, Q. L. (2023). Dynamic mechanical mechanism and optimization approach of roadway surrounding coal water infusion for dynamic disaster prevention. *Measurement, 223*, 113639.

Haghighat, A. E. (2015). Diffraction of Rayleigh wave by simple surface irregularity using boundary element method. *Journal of Geophysics and Engineering, 12*(3), 365–375.

Hong, Z. X., Tao, M., Cui, X. J., Wu, C. Q., & Zhao, M. S. (2022). Experimental and numerical studies of the blast-induced overbreak and underbreak in underground roadways. *Underground Space, 8*(1), 61–79.

Jeon, S., Kim, J., Seo, Y., & Hong, C. (2004). Effect of a fault and weak plane on the stability of a tunnel in rock—a scaled model test and numerical analysis. *International Journal of Rock Mechanics and Mining Sciences, 41*(S1), 658–663.

Jiang, Q., Feng, X. T., Chen, J., Huang, K., & Jiang, Y. L. (2013). Estimating in-situ rock stress from spalling veins: A case study. *Engineering Geology, 152*(1), 38–47.

Lee, V. W., & Karl, J. (1992). Diffraction of SV waves by underground, circular, cylindrical cavities. *Soil Dynamics and Earthquake Engineering, 11*(8), 445–456.

Li, C. J., & Li, X. B. (2018). Influence of wavelength-to-tunnel-diameter ratio on dynamic response of underground tunnels subjected to blasting loads. *International Journal of Rock Mechanics and Mining Sciences, 112*, 323–338.

Li, W. T., & Chen, Q. J. (2020). Effect of vertical ground motions and overburden depth on the seismic responses of large underground structures. *Engineering Structures, 205*, 110073.

Li, X. B., Cao, W. Z., Tao, M., Zhou, Z. L., & Chen, Z. H. (2016). Influence of unloading disturbance on adjacent tunnels. *International Journal of Rock Mechanics and Mining Sciences, 84*, 10–24.

Li, X. B., & Weng, L. (2016). Numerical investigation on fracturing behaviors of deep-buried opening under dynamic disturbance. *Tunnelling and Underground Space Technology, 54*, 61–72.

Li, X. D., Liu, K. W., Yang, J. C., Sha, Y. Y., & Song, R. T. (2023). Numerical study on the effect of in-situ stress on smoothwall blasting in deep tunnelling. *Underground Space, 11*, 96–115.

Liu, D. K., Gai, B. Z., & Tao, G. Y. (1980). On dynamic stress concentration in the neighborhood of a cavity. *Earthquake Engineering and Engineering Vibration, 1*, 97–110 (in Chinese).

Liu, Z. X., Ju, X., Wu, C. Q., & Liang, J. W. (2017). Scattering of plane P1 waves and dynamic stress concentration by a lined tunnel in a fluid-saturated poroelastic half-space. *Tunnelling and Underground Space Technology, 67*, 71–84.

Lu, W. B., Yang, J. H., Yan, P., Chen, M., Zhou, C. B., Luo, Y., & Jin, L. (2012). Dynamic response of rock mass induced by the transient release of in-situ stress. *International Journal of Rock Mechanics and Mining Sciences, 53*, 129–141.

Luo, H., Tao, M., Wu, C. Q., & Cao, W. Z. (2023). Dynamic response of an elliptic cylinder inclusion with imperfect interfaces subjected to plane SH wave. *Geomechanics and Geophysics for Geo-Energy and Geo-Resources, 9*, 24.

Mitelman, A., & Elmo, D. (2014). Modelling of blast-induced damage in tunnels using a hybrid finite-discrete numerical approach. *Journal of Rock Mechanics and Geotechnical Engineering, 6*, 565–573.

Panji, M., Mojtabazadeh-Hasanlouei, S., & Fakhravar, A. (2022). Seismic response of the ground surface including underground horseshoe-shaped cavity. *Transportation Infrastructure Geotechnology, 9*, 338–355.

Pao, Y., & Mow, C. (1973). Diffraction of elastic waves and dynamic stress concentrations. *Journal of Applied Mechanics, 40*(4), 872.

Shen, Y. S., Gao, B., Yang, X. M., & Tao, S. J. (2014). Seismic damage mechanism and dynamic deformation characteristic analysis of mountain tunnel after Wenchuan earthquake. *Engineering Geology, 180*, 85–98.

Su, G. S., Feng, X. T., Wang, J. H., Jiang, J. Q., & Hu, L. H. (2017). Experimental study of remotely triggered rockburst induced by a tunnel axial dynamic disturbance under true-triaxial conditions. *Rock Mechanics and Rock Engineering, 50*, 2207–2226.

Tao, M., Li, Z. W., Cao, W. Z., Li, X. B., & Wu, C. Q. (2019). Stress redistribution of dynamic loading incident with arbitrary waveform through a circular cavity. *International Journal for Numerical and Analytical Methods in Geomechanics, 43*(6), 1279–1299.

Tao, M., Zhao, H. T., Li, X. B., Li, X., & Du, K. (2018). Failure characteristics and stress distribution of pre-stressed rock specimen with circular cavity subjected to dynamic loading. *Tunnelling and Underground Space Technology, 81*, 1–15.

Tao, M., Zhao, R., Du, K., Cao, W. Z., & Li, Z. W. (2020). Dynamic stress concentration and failure characteristics around elliptical cavity subjected to impact loading. *International Journal of Solids and Structures, 191*, 401–417.

Wang, T., Fan, B. W., & Khadka, S. S. (2020). Flowchart of DEM modeling stability analysis of large underground powerhouse caverns. *Advances in Civil Engineering, 2020*, 8874120.

Xia, Y., Jin, Y., Chen, M., & Lu, Y. H. (2017). Dynamic analysis of a cylindrical casing-cement structure in a poroelastic stratum. *International Journal for Numerical and Analytical Methods in Geomechanics, 41*(12), 1362–1389.

Xiang, G. L., Tao, M., Zhao, R., Zhao, H. T., Memon, M. B., & Wu, C. Q. (2024). Dynamic response of water-rich tunnel subjected to plane P wave considering excavation induced damage zone. *Underground Space, 15*, 113–130.

Zhao, H. T., Tao, M., & Li, X. B. (2023a). Theoretical analysis of dynamic stress distribution around a circular damaged roadway under transient disturbance. *International Journal for Numerical and Analytical Methods in Geomechanics, 47*(17), 3248–3265.

Zhao, R., Tao, M., Wu, C. Q., Wang, S. F., & Zhu, J. B. (2023b). Spallation damage of underground openings caused by excavation disturbance of adjacent tunnels. *Tunnelling and Underground Space Technology, 132*(5), 104892.